MODELING THE EFFECT OF *IN SITU* NOZZLE-INTEGRATED COMPRESSION ROLLING ON THE MECHANICAL AND FRACTURE BEHAVIOR OF FUSED FILAMENT FABRICATION (FFF) 3D PRINTED PARTS

BY

MOMEN M. QASAIMEH

Presented to the Faculty of the Graduate School of

The University of Texas at Arlington in Partial Fulfillment of the Requirements for the Degree of

DOCTOR OF PHILOSOPHY

THE UNIVERSITY OF TEXAS AT ARLINGTON

DEPARTMENT OF MECHANICAL AND AEROSPACE ENGINEERING

AUGUST 2021

ACKNOWLEDGMENTS

Ph.D. is a long life journey and a strenuous mission that can be impossible without economic, emotional, and academic support from significant people in my life.

First, I'd like to acknowledge my supervising professor Dr. Ashfaq Adnan for his support and orientations during my study. He never hesitated to provide all possible help.

Also, I'd like to thank my wife, Aseel Al-Shorman, for standing next to me and trying her best to ensure the best studying atmosphere.

Finally, I will never forget my parents, Dad, and Mum, who supported me from the beginning of my life.

DEDICATION

To my soul mate, Aseel Alshorman.

Abstract

MODELING THE EFFECT OF *IN SITU* NOZZLE-INTEGRATED COMPRESSION ROLLING ON THE MECHANICAL AND FRACTURE BEHAVIOR OF FUSED FILAMENT FABRICATION (FFF) 3D PRINTED PARTS

Momen M. Qasaimeh, PhD

The University of Texas at Arlington,
August 2021

Supervising Professor: Dr. Ashfaq Adnan

Fused filament fabrication (FFF) is one of the most common additive manufacturing/3D printing techniques where continuously extruded semi-molten filaments are deposited in a layer-by-layer manner. The quality of the manufactured part depends on some major factors such as filament-filament contact and adhesion as well as the void fraction. Filament to filament adhesion affects the part strength under transverse load. In our earlier work, we studied the effect of in situ ball rolling on the thermal and mechanical properties of the printed parts. It was found that when printing/rolling parameters are correctly tuned and *in situ* compression rolling is appropriately applied over the depositing filaments, a significant increase in material toughness and tensile strength are realized. Here, we have developed an integrated model that includes the *in situ* compression rolling and filament-filament contact during deposition. The rolling parameters such as ball weight, ball temperature, filament temperature are explicitly included in the model. The effect of these parameters on the part height, void fraction, and filament adhesion are studied. Based on JKR contact theory and the theory of elasticity, our mathematical model predicts the

evolution of filament-to-filament contact width and corresponding void fraction and part height in the representative volume element of the simulated printed part. Our prediction matches fairly well with the previous experimental results. We have also optimized the filament temperature during the rolling process. We find that the maximum adhesion between filaments occurs when the two filaments are brought close to isothermal contact. We have concluded that parts fabricated from a system integrated with an in-situ preheating and in situ post-rolling would yield the most effective part.

The next step to fulfill this research's scope is to study the fracture behavior of printed filaments in contact. We have considered the effect of the contact half-width and the impact of the shape of the filament cross-section (filaments mesostructured) on the fracture strength and on mode I stress intensity factor (SIF) at the crack tip. The results show that the rolled filaments have a longer contact half-width and larger notch angle at the interface between the filaments, which means higher singularity order and better fracture properties. A 3 point bending test has been conducted to measure the fracture strength for rolled and baseline v-notch samples. The rolled part's strength shows double the baseline part strength. A computational study has been formed to predict fracture behavior. We found that at longer filament-filament contact width, the part has a higher critical stress intensity factor and slower crack propagation. We believe that studying the fracture behavior of the printed filaments under different temperatures will add significant knowledge to industrial applications like 3d printed electronic devices or 3d printed heat exchangers. So, we have tested the rolled part's strength at different temperatures. As expected, the temperature increase results in less fracture strength and more ductile behavior.

Contents

Chapter 1
Introduction

The deposition of semi-molten polymer filaments in a layer-by-layer manner to form desired parts is a new manufacturing method known as additive manufacturing (AM) or 3D printing. AM offers several advantages over the traditional manufacturing techniques, in particular for rapid prototyping. The process is economical, simple to implement, and time-saver. Filament fused fabrication FFF is one of the most commonly used 3D printing methods for polymer fabrication. In FFF, process parameters such as printing speed, cooling rate, and layer thickness play an essential role in the quality of printed parts (Popescu et al., 2018).

1.1 Materials

To appropriately tune the process parameters, understanding the printing material's physical and mechanical properties is essential (Ngo et al., 2018). Thermoplastics is a well-known material for thermoforming applications (Schaul, 1985). Its ability to soften upon heating and hardening upon cooling without changing chemical properties makes it a suitable material for FFF 3D printing (Diegel et al., 2019). Polylactic acid (PLA) is a widely used biodegradable thermoplastic material in widespread industrial applications (Farah et al., 2016). The low softening temperature of PLA makes it the right candidate for 3D printing (Valerga et al., 2018). As such, several studies have been conducted with PLA as a printing material. Significant efforts have been made to obtain the best printing and environmental conditions for PLA parts (Abeykoon et al., 2020) (Valerga et al., 2018) (Zhao et al., 2019)(Corapi et al., 2019). Various pre-and post-process techniques have

been adopted to improve the printed material's mechanical properties (Rane et al., 2020) (Diegel et al., 2019). Recently, innovative processes such as *in situ* heating or *in situ* filament compression have demonstrated significant improvement in part quality and properties (Ravoori et al., 2019a) (Ravi et al., 2016) (Prajapati et al., 2021).

1.2 3D printing process

Although it's a promising new technology, 3D printing still requires further research and innovation. 3D printed part suffers from poor thermal and mechanical properties due to its anisotropy behavior (Prajapati et al., 2018). The filament depositing process often leaves gaps or voids between adjacent filaments. Those voids lead to porous structures and degraded mechanical behavior (Popescu et al., 2018). Reducing the fraction of these gaps is an active research goal (Patanwala et al., n.d.). Filament to filament adhesion is another concern. As the filament is deposited, it cools and solidifies instantly. When the second layer of filament is deposited adjacent to or over the previously deposited layer, the heat from the printing nozzle, along with the heat from the newly deposited filament, keeps the deposited filaments in a softened state. The degree of softness (i.e., semi-molten state) of the adjoining filaments controls overall adhesion between filaments. (Costa et al., 2017). As such, understanding adhesion helps in improving the mechanical properties of the printed parts. When two thermoplastic materials come to contact, the degree of adhesion is mainly controlled by polymer chains' inter-diffusion between the two contacting surfaces. The mobility of the polymer chains increases with temperature. This temperature effect makes it essential to ensure that both surfaces are at elevated temperatures to enhance the adhesion. The concept of providing additional *in situ* heat to maintain the required chain plays a significant

role in improving the mechanical properties of the printed parts. (Yang & Pitchumani, 2002) (Seppala et al., 2017)

1.3 Fracture behavior of 3d printed parts

The fracture behavior of 3d printed parts has been studied broadly in the literature. (Rezaee & Adnan, 2018a) studied the elastic stress singularities and mode I notch stress intensity factor (SIF) for 3D printed polymers. The study took into account the singularities created when the fused filament fabrication was used (FFF). The researchers used the stress intensity factor approach to analyze the effect of the singularity points. They found that the main two parameters that affect the FFF parts' fracture properties were the length of the interface and the opening angle of the singular points. (Fonseca et al., 2019) studied the interlaminar fracture under mode I loading. They found that the material fracture toughness was higher for the reinforced PA than pure PA. (Aliheidari et al., 2017) submitted a method to study the fracture resistance and interlayer adhesion of FFF printed parts. They noticed that the load increased linearly before the crack initiation and nonlinearly after the crack initiation occurred. They also found that the fracture critical load increased when the printing nozzle temperature increased. (Hart & Wetzel, 2017) studied the fracture behavior of additively manufactured ABS material. The authors found that the J_{1c} value was significantly higher for the cross laminar fracture test than the J_{1c} value for the inter-laminar fracture test. They explained this difference in fracture toughness happened because of the low strength of the inter-laminar bonds. (Ahmed & Susmel, 2017) considered the infill orientation as the most important printing parameter. They studied its effect on the fracture toughness and the static strength of the 3D printed specimen. They conclude that the crack has two main mechanisms. Initially, the crack occurred between the filaments and is dominated by shear stress. After that, the

crack took place on the filament, which is dominated by the normal stress. They found that the infill orientation does not significantly affect the mechanical and fracture behavior when the specimens are printed horizontally.

In a related research field, improving the fracture toughness of 3d printed parts has gotten attention. A study conducted by (Gardan et al., 2018) aimed to improve the fracture resistance of FFF 3D printed specimens by adopting a new extrusion deposition strategy. This new strategy was developed by regenerating the principal stress directions inside the 3D printed part. It was found that the newly designed specimen was stronger under tensile loading than the classical specimen, where the fracture resistance was 20% higher. It was noticed that the crack propagation was significantly affected by the new filament orientation. (Dunn et al., 2019) investigated the effect of annealing 3d printed parts on improving the fracture behavior. They found that annealed parts have 1800% higher fracture toughness and exhibit ductile fracture with plastic deformation, unlike the baseline samples, which have lower fracture toughness and fracture propagated between the printed layers.

1.4 Earlier studies

Experimental studies occupy the lion's share in studying the behavior and performance of 3d printed parts. Modeling of 3D printing process helps in optimizing the process-structure relation and print quality. In the open literature, very few mathematical models have been found (Enrique Cuan-Urquizo et al., 2019). A couple of researchers used available theories like laminate plate theory (Casavola et al., 2016) (Kulkarni & Dutta, 1999) (Ziemian et al., 2016), and the micromechanics approach (E. Cuan-Urquizo et al., 2015) (Huang & Singamneni, 2015) to describe process-structure relation and to improve the performance of 3d printed parts. Computational-

based studies can also be found in the literature (Enrique Cuan-Urquizo et al., 2019) (Brenken, 2017). The finite element technique has been implemented to model the printing process and to predict the properties of printed parts (Enrique Cuan-Urquizo et al., 2019). (Brenken, 2017) conducted a study to predict the residual stresses and final deformation of large-scale 3d printed parts. He used several concepts like heat transfer, crystallization, viscoelasticity, and material shrinkage. He pointed out the importance of include the viscoelastic behavior in such a model.

Yet, there is still a large gap in the previous research related to mathematical investigations of the quality and properties of 3d printed pieces. As it comes to our knowledge, the research lacks modeling and predicting the mechanical behavior and fracture behavior of 3D printed thermoplastic material under different environmental conditions.

1.5 Scope of current research

In this work, we have employed a contact mechanics-based mathematical model to predict the contact width, and the corresponding void fraction in 3d printed PLA parts. The effects of surface energy and *in situ* compression ball rolling are considered. In the previous study (Ravoori et al., 2021), an experimental setup of *in situ* compression was created by integrating a ball roller to move along before and after the printing nozzle. This roller applied a compression load on the filament while it is still hot and soft. We have observed that the *in situ* compression alters the deposited filaments' cross-section and the filament-filament contact width. A significant decrease in void fraction has been noticed as well. We found that the material toughness and tensile strength of the in situ rolled samples are considerably higher than the baseline unrolled samples (Ravoori et al., 2021). This encourages us to further investigate the contact behavior of the filaments under compression by utilizing a mathematical model to better understand the material behavior under

rolling. Also, to predict the mesostructure and the final height of the printed/rolled parts. We believe this study provides a fundamental understanding of the adhesion between the filaments and void reduction in the printed parts. Furthermore, we intend to study the fracture behavior of the 3d printed/rolled parts and how well the rolling after printing results in improving the fracture and cracking behavior under mode I loading.

1.6 PLA material

In the current research, in order to model the printing material's behavior under different temperatures, we need to know several of the mechanical and thermal properties of the material which is chosen to be PLA. The thermal conductivity of PLA does not change dramatically with temperature below the melting point. Linear interpolation can be used to find the conductivity values at specific temperatures by using the available values in the open literature (Jamshidian et al., 2010). A summary of the properties of the used material can be found in appendix B.

1.7 Adhesion and bonding

One of the important parameters in our model is the work of adhesion. The work of adhesion, in case the materials in contact are the same, is equal to twice the surface energy. The reported surface energy of PLA is equal to 0.0416 J/m^2. As such, the PLA-PLA work of adhesion is equal to 0.0832 J/m^2 (Yousefzade et al., 2019) (Biresaw & Carriere, 2001). On the other hand, the adhesion of two different materials is more complicated. Polymer to metal sticking needs to be maximized in some industrial applications like metal-polymer composites and needs to be minimized in other applications like in polymer rolling or drawing.

A couple of research has studied polymer-metal interaction and bonding by using molecular dynamics simulation. The physical properties of the polymer play a great role in metal-polymer non-bonding adhesion. Longer polymer chains and higher chain flexibility increase the energy of adhesion (Suérez et al., 2008). In another study (Kisin et al., 2007), the thermodynamics work of adhesion between metallic and polymeric surfaces has been studied by simulating the interactions between ABS and copper. This study provides a good understanding of the polymer-metal adhesion mechanism (Kisin et al., 2007). The average value of the work of adhesion in this study has been adopted as a good estimation for the work of adhesion in the current research (1.93 J/m^2). In our case, the goal is to minimize the steel ball adhesion to PLA filaments. As the ball temperature increase, it will result in increasing the adhesion with the filament (Bechtel et al., n.d.) (M. Zhou et al., 2020). So, elevated rolling ball temperature will increase the layer surface roughness and result in lousy adhesion, as previously observed (Ravoori et al., 2021). On the other hand, low ball temperature will result in cooling the filament, which is not preferable (Costa et al., 2017) (Solarski et al., 2007). These observations led us to choose the ball temperature to be 110℃ in our model. This temperature has been experimentally investigated to be optimal (Ravoori et al., 2021) and can also be indicated from a research study for other similar applications (Solarski et al., 2007).

Chapter 2

Mathematical Modeling of 3d Printing and Compression Rolling Process by Using Contact Mechanics

2.1 Introduction

Contact mechanics theories study the behavior of two bodies in contact. The cornerstone of the contact mechanics has been originated with the first observations by Hertz (K. L. Johnson (1985)). Later, other theories came out to describe the behavior of two bodies in contact in more detail. JKR theory discusses the adhesive contact between two elastic solids. It investigates the effect of surface energy on the contact width of two bodies in contact (Johnson et al., 1971). Among other contact theories, JKR is an adequate theory for examining the behavior of two soft bodies in contact. It assumes that the contact stresses only act along the contact width, which means no stresses outside the contact width (Ciavarella et al., 2019).

2.2 Model formation

In our earlier work (Ravoori et al., 2021), three compression balls were assembled over each other to apply a compression load on a just deposited PLA filament. Each ball has 9 grams mass and 12 mm diameter and is made from 44C Stainless Steel. The temperature of the balls was

maintained at 110℃. A high-speed camera has been used to measure the filament height during printing. Deposited filament profiles as a function of time have been plotted by using infrared imaging for rolling and no rolling cases. The rolling ball was located 17 mm far from the printing nozzle. It implies that the compression rolling was felt approximately 1 second after filament deposition and at around 130℃ filament temperature. The effect of printing/rolling speed, rolling ball temperature, compression load, and pre/post/dual rolling configuration were considered (Ravoori et al., 2021). In the current study, we have set up a computational model that incorporates the post rolling configuration and three rolling balls assembled to apply the compression load after the printing nozzle, as illustrated in the following figure. The filaments are modeled as two cylinders are in contact.

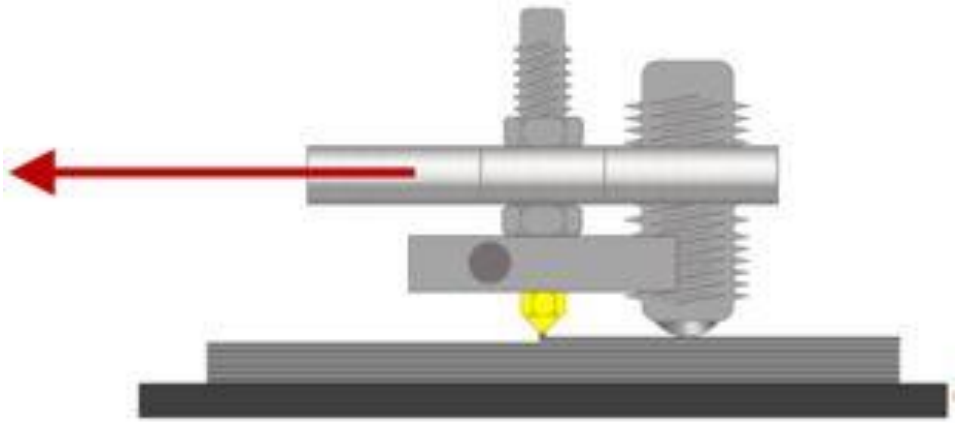

Figure 1: Schematics of 3D printing process with an integrated in-situ ball rolling to apply compression load over the just deposited filament while it is still hot and soft. (Ravoori et al., 2021).

We need to match the experimental conditions; two different temperatures are set for the two cylinders. The contact between the cylinders is maintained by a mechanical pressure load

distributed over the contact area (Peng & Huang, 2016). We consider four different configurations based on the provided infrared images of the printing/rolling process from the previous work (Ravoori et al., 2021). In case # 1, we have a steel ball at 110℃ in contact with a PLA filament at 130℃. This case represents the first turn of the ball rolling over a single filament. In case # 2, we have two PLA filaments in contact under the applied pressure from the weight of the steel ball. The upper filament is at 130℃, while the lower filament is at 90℃. This case represents the second turn of rolling over two filaments. Case #1 and case #2 collectively represent the effect of ball rolling on the contact width between the first two deposited filaments. Steps of case # 2 will be repeated between the upcoming filaments across the filament thickness. The roller's effect will be assumed negligible after the second turn of rolling passes over the first deposited filament because as time evolves, the first filament becomes far from the heating sources and most likely remain undeformable.

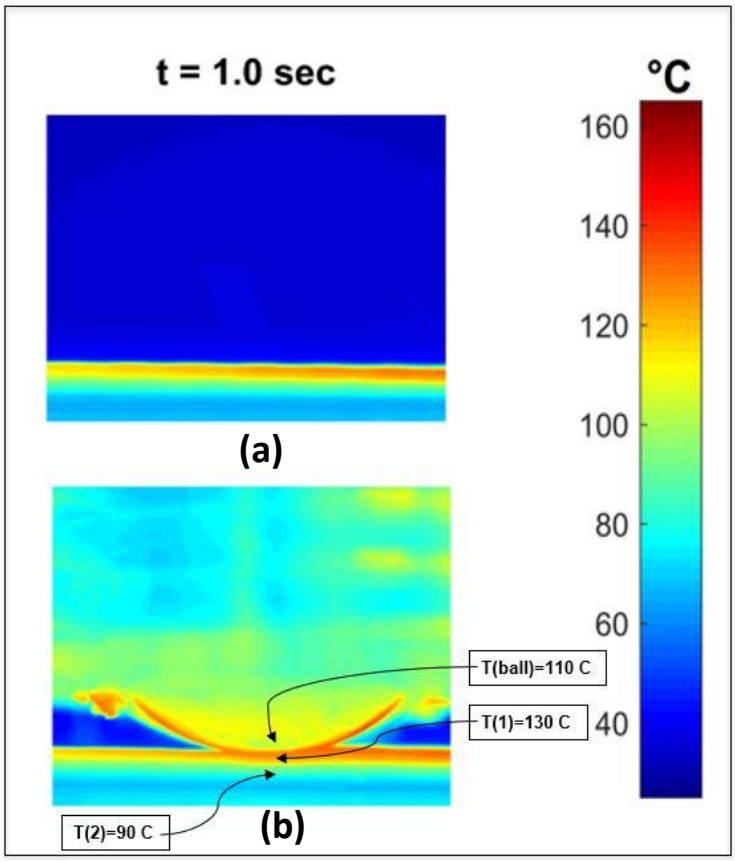

Figure 2: Schematics of (a) Filaments temperature for no rolling case (b) The ball and the two filaments temperature for in-situ ball rolling after printing(Ravoori et al., 2021).

Case # 3 considers two filaments with no ball rolling, and the applied load is only the weight of the upper filament. The upper filament is at 130℃, while the lower filament is at 90℃. We have established this case to compare the results of rolling with no rolling cases. Finally, in case # 4, we study the filament to filament contact in the lateral direction where the two filaments are placed adjacent to each other with no load applied, as illustrated in figure 4.

We work on the hypothesis that rolling PLA filament immediately after deposition while the filament is still hot, soft, and flexible will lead to deformation and reshaping of the filament cross-

section in a way that will promote filament-filament adhesion. Let us assume that the filament after deposition has a circular cross-section with a diameter equal to the printing nozzle diameter. We assume that the filament cross-section will evolve with time and will eventually look like the shape shown in figure 3.b (Coogan & Kazmer, 2019). The new shape is a result of flattening of the circular cross-section and is characterized by three geometric parameters, a and R, as shown in Fig 3b. Our goal is to find the numerical values for a and R under the applied load P.

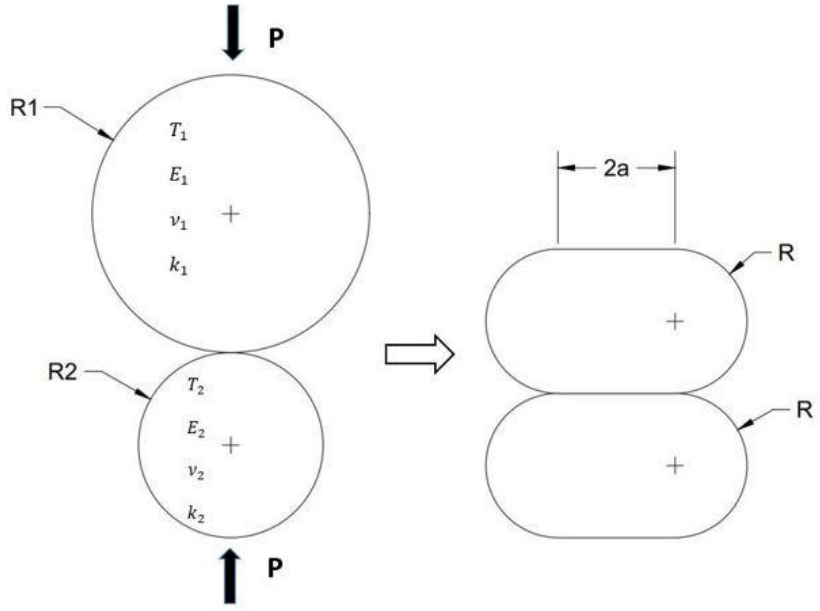

Figure 3: (a) Expected filament cross-section shape Before rolling; (b) Expected filament cross-section shape after rolling

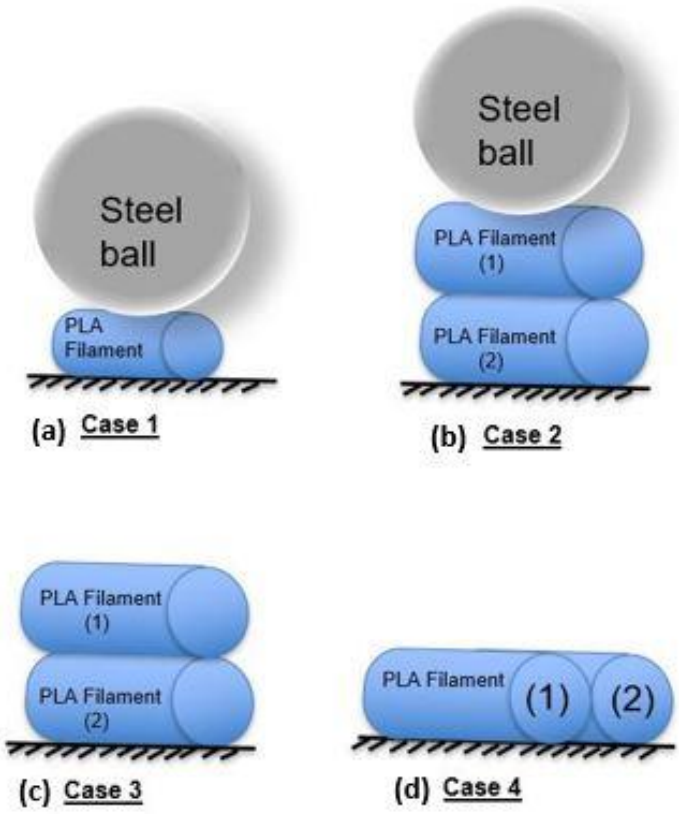

Figure 4: (a) Schematics of a steel ball at 110℃ in contact with PLA filament at 130℃; (b) Picture of two PLA filaments in contact under the applied pressure which comes from the steel ball weight; (c) Schematics of two filaments with no ball rolling and the applied load is only the weight of the upper filament; (d) Illustration of the filament to filament contact in the lateral direction where the two filaments are beside each other with no load applied.

2.3 Mathematical formulation

Let us consider a general case where we have two cylinders with two different diameters. The two cylinders are in contact non-isothermally under the externally applied load P measured as force per unit length (in N/m). We assume that the cylinders exhibit linear elastic isotropic material

properties. The cylinders have a uniform temperature, and the heat transfers in one direction across the contact width ($|X| < a \ \& \ Y = 0$) from the hot upper cylinder to the cold lower one, as shown in figure 5. The JKR adhesive contact theory states that the strain release rate of crack propagation in a brittle material G can be equated with the work of adhesion $\Delta\gamma$ between the two surfaces with two different temperatures (Johnson et al., 1971) (Peng & Huang, 2016). Therefore,

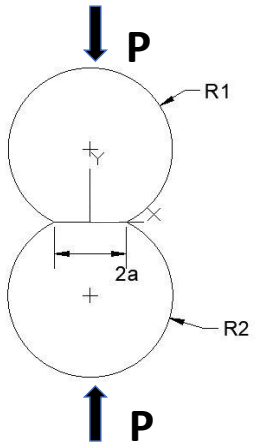

Figure 5: Schematics of two cylinders in contact, the upper cylinder is hotter, and the lower cylinder is cooler, under P applied pressure and 2a contact width.

We find the mathematical relation between the applied load and the contact half-width as follows:

$$P = \frac{\pi E^*}{4R^*}a^2 + \frac{E^*\varepsilon_1}{C}a + \sqrt{(2\pi\Delta\gamma E^*)a - \frac{(\pi E^*\varepsilon_2)^2}{4}a^2} \quad (1)$$

Detailed derivation can be found in appendix A. In the next section, we will employ the mathematical equations to find the contact half-width of all of the cases shown in figure 4.

2.4 Experiment and materials

To feed our mathematical model, we have conducted supporting experiments to find the modulus of elasticity of PLA at various temperatures. To run our experiments, we have connected a thermal chamber to a Shimadzu AGS-X series universal testing machine with a 5 kN load cell and a pair of mechanical grips with a cross-head speed of 0.02 mm/min. The results are plotted and shown in figure 6. The results agree very well with other reported studies (C. Zhou et al., 2016), in particular, between a range of temperatures from 20℃ to 175℃. We have used the elasticity values at 90℃ and 130℃ in our model, which is equal to 20 MPa and 75 MPa, respectively. Appendix A summarizes the required thermal and mechanical properties for PLA filaments at 130℃ and 90℃. We have also included the properties of the still ball we used as a roller.

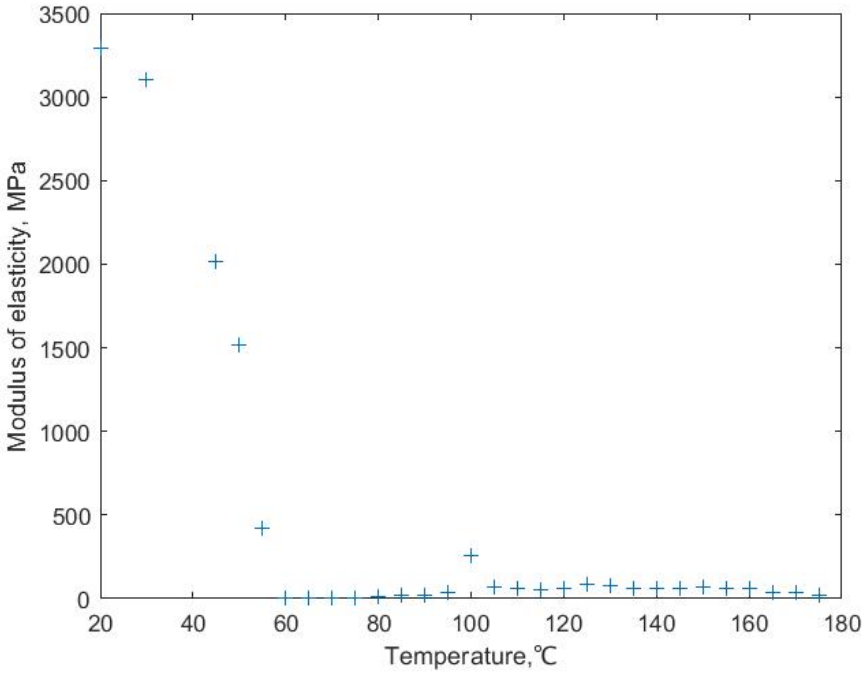

Figure 6: Modulus of elasticity (E) for PLA filament at different temperature values.

Chapter 3

The Contact Half-Width of 3d Printed Filaments for Rolling and No Rolling Conditions

Applying the numerical values of the material properties discussed into the mathematical equations outlined will give us the contact half-width of each interacting "filament" cylinder, as shown in figure 4. Four different cases have been considered – (a) two hot filaments in contact subjected to *in situ* compression from the steel ball weight; (b) two hot filaments in contact without the compression ball, and the applied load is only the weight of the upper filament; (d) filament to filament contact in the lateral direction where the two filaments are beside each other with no load applied. Illustration diagrams and plots for this chapter can be found in appendix C.

3.1 Results of case 1, Ball-filament contact

As illustrated earlier, case one represents the effect of a ball rolling over a single filament. In order to study this case, we apply the mathematical model represented by equation 28 (Appendix A) to correlate the applied load as a function of the half-width.

To verify our model, we have revisited the experimental procedure and set up of the previous work (Ravoori et al., 2021). In this study, we printed the first layer with a layer height equal to 0.2 mm to provide better adhesion with the printing bed. In our model, we have assumed $R_2 = 0.1$ mm, which represents the radius of the first printed/rolled filament.

We assume that the applied force P (force/width) is distributed uniformly over the in-plane direction of the contact area to simplify the solution. We have also considered that the contact area under the applied pressure has a flat shape with an edge length equal to 2a. With these assumptions, the parameter 'a' is obtained by solving equation 28 (Appendix A). Assuming F (in Newton) equal to the equivalent force applied on the contact area, then we rewrite equation 28 (Appendix A) in the form:

$$F = 2a \times P = 2a \times \left[\frac{\pi E^*}{4R^*} a^2 + \frac{E^* \varepsilon_1}{C} a + \sqrt{(2\pi \Delta \gamma E^*) a - \frac{(\pi E^* \varepsilon_2)^2}{4} a^2} \right] \quad (2)$$

Where F is the equivalent force applied over the contact area in Newtons.

Once we obtain the half-width of the contact between the steel ball and the PLA filament, we plot F versus 'a'. The desired value of the contact half-width 'a' corresponds to the applied load F. In this case, the applied load F is equivalent to the weight of the three balls (0.2 N). Accordingly, the half-width a = 5.573×10^{-5} m, as shown in appendix c.

It is evident that our general problem is to solve for the contact width between two cylinders subjected to an applied load. The area of two cylinders in contact has a rectangular shape (Williams & Dwyer-Joyce, 2000). In the current case, the rollerball is 15 times larger in diameter than the filament. In theory, the area pressed by a rigid ball on an elastic media has an oval shape (K. L. Johnson, 1985). In our case, we have a ball rolling over a cylindrical filament. Let assume that the ball rolled over the plate from position A (the hatched green area in figure 7) to B (the hatched yellow area in figure 7). Then, the rolled area's projection will look like the total hatched area. To simplify our calculations, we assume that the contact area while rolling has a triangular shape like

the red triangle in figure 7. The center mass of the rolling ball is applied over the triangle centroid. To correct our findings, we use the previous result for (a) with a correction factor equal (2/3).

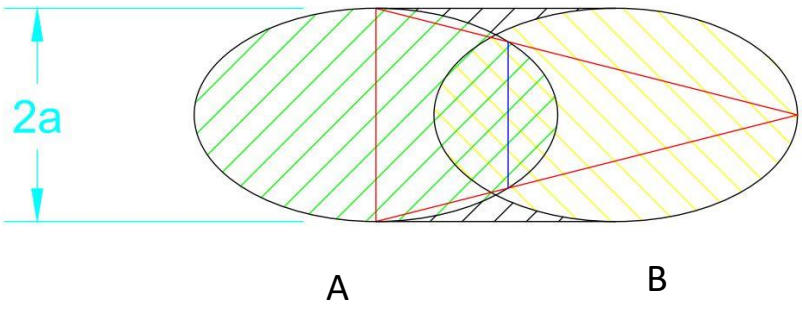

Figure 7: A schematic diagram to illustrate the area of contact in case a rigid ball is rolling over an elastic cylinder.

So the corrected value for a = 0.037 mm. Following the assumption, which states that the ball rolling will reshape the filament cross-section, we applied the Pythagoras theorem to find the filament height "h" after the first rolling pass. For a = 0.037 mm and R = 0.1 mm, we find h = 0.093 mm, assuming that the original filament diameter before rolling is equal to the filament height 0.2 mm, then the change in filament diameter/height is equal to $\Delta H_1 = 0.014$ mm, as shown in figure 8. So the final filament height for case 1 (H) will be equal to 2h. Similarly, we can apply the same procedure to find the filament height for other cases.

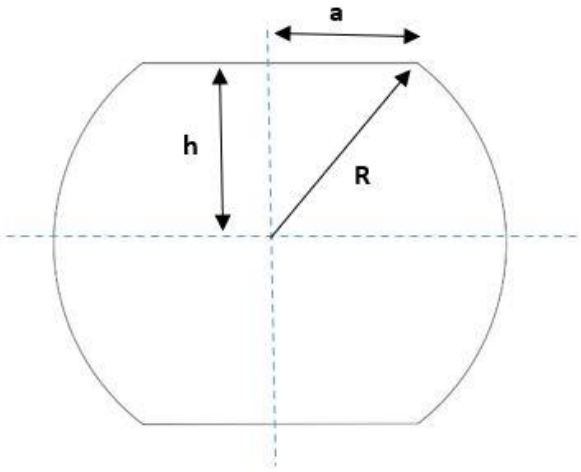

Figure 8: Illustration diagram for the expected filament cross-section after rolling.

3.2 Results of case 2, with rolling filament-filament contact

Similarly, in this case, we have two PLA filaments in contact. This case will be divided into two parts; the first one represents the contact between the first printed/rolled part, which has a 0.1 mm radius, with the second one, which has 0.2 mm. The radius of the first filament sets to be equal to 0.1 mm because, as we have mentioned earlier, in our previous work, the first filament has been printed with 0.2 mm height to provide better adhesion between the first layer of the printed material and the printing bed. The second part of this case represents all other filaments that are printed after the first layer. All these filaments are assumed to have the same radius before rolling R = 0.2 mm, which equals the printing nozzle radius.

Similar to the previous case, we assume that the projection of the filament-to-filament contact has a square area. This area represents the contact area that is subjected to the pressure load (the ball weight). Then, we plot F as a function of 'a'. By knowing 'a', we can calculate the filament height after rolling.

We find that a = 7.53×10^{-5}m. Again, we can apply the Pythagoras theory to find the change in

the filament height "h" after rolling. For a = 0.075 mm and for R = 0.2 mm we find h = 0.185 mm. The corresponding change in the height $\Delta H_2 = 0.029$ mm. In part two of this case, we have the two filaments in contact with the same diameter before rolling, which is equal to the nozzle diameter. Both filaments have their radius R = 0.2 mm. Then from F vs. a plot, we can obtain the contact half-width a = 8.66×10^{-5} m.

Again, we use the Pythagoras theorem to find the filament height after the second rolling pass. For a = 0.087 mm and R = 0.2 mm, we find h = 0.180 mm. assuming that the original filament diameter before rolling equal the printing nozzle diameter 0.4 mm, then the change in filament diameter/height is equal to $\mathbf{\Delta H_3} = 0.039$ mm. This result applies to the next two filaments.

Therefore, to find the net change in filament to filament height $\mathbf{\Delta H}$ after four passes of printing/rolling, we have added the results from case one and the results of the two parts of case two: $\mathbf{\Delta H = \Delta H_1 + \Delta H_2 + 2\Delta H_3} = 0.121$ mm.

For the scenario when we have no rolling, the filaments will not deform. Then the height of the four filaments, $\mathbf{H_{no\ rolling}}$ = 0.2 +3 (0.4) = 1.4 mm. If we subtract $\mathbf{H_{no\ rolling}}$ from $\mathbf{\Delta H}$, then the net change in the filament height due to rolling alone would be $\mathbf{H_{rolling} = H_{no\ rolling} - \Delta H}$ = 1.279 mm. To verify our result, we compare it with the measured value for the four printed/rolled layers from the previous experimental work (Ravoori et al., 2021). The experimental value for the filament height due to rolling, $\mathbf{H_{rolling,ex} = 1.21}$ mm. The percentage error in our predicted value is equal to 5.4%, which is certainly insignificant. As such, it can be inferred that our model can quantitatively predict the height of the 3D printed part with a ball rolling.

3.3 Results of case 3, no rolling filament-filament contact

In this case, we intend to study the filament deformation if there is no rolling. According to previous observations (Ravoori et al., 2021), we believe that the filament deforms over each other even if there is no rolling pressure applied. In this case, we study the effect of the filament weight on the contact width of two PLA filaments in contact. We use the same model, but this time the applied load is the upper filament weight. Similarly, to compare with our previous experimental work, we have kept the setup consistent.

This case has two parts, such as case 2. The first part represents the contact between the first printed filament and the second one, where the diameter of the first filament is 0.2 mm (for better adhesion with printing bed). The second part represents the contact between the rest of the printed filaments after the first layer with a 0.4 mm diameter. Again, we plot F as a function of the contact half-width. Here, F represents the weight of the 7-cm long PLA filament. We use the filament length to be equal to 7 cm because it is equivalent to the length of the Dogbone test coupons, which we have tested in the previous experimental work (Ravoori et al., 2021). We calculate the filament weight by multiplying the filament volume by its density.

$$\mathbf{F} = \boldsymbol{\rho} \times \mathbf{V} = \boldsymbol{\rho} \times (\boldsymbol{\pi} \mathbf{R^2 L}) \qquad (\mathbf{3})$$

Where $\boldsymbol{\rho} = \mathbf{1.36} \frac{\mathbf{g}}{\mathbf{cm}}$ is the PLA density (Herrera Franco & Valadez-González, 2005). V is the filament volume, R is the filament radius, and L is the filament length. Substitute numbers we can find the filament weight F = 0.00012 N. For part one, we have the first filament diameter equals 0.2 mm and the second filament diameter equals 0.4 mm. Then, we obtain the contact half-width value a = 8.31$\times \mathbf{10^{-6}}$ m. Like before, for a = 0.00831 mm and R = 0.1 mm, we find h = 0.0997 mm, and $\boldsymbol{\Delta H_1} =$ 0.0007 mm. For part two, we have the first filament diameter equals 0.4 mm and the second filament diameter equals 0.4 mm.

Now, we can obtain the contact half-width value a = 1.0115× $\mathbf{10^{-5}}$ m. Similarly, For a = 0.01012 mm and R = 0.2, we find h = 0.1997 mm and $\Delta\mathbf{H_2} = 0.0006$ mm. This result applies to the next two filaments. Therefore, to find the net change after four passes of the printing nozzle, we need to include the results from part one and part two to find the final change in the height of the filament $\Delta\mathbf{H} = \Delta\mathbf{H_1} + \mathbf{3}\Delta\mathbf{H_2} = 0.0025$ mm.

If we compare this result with the ideal case, which assumes that the filaments will not deform. Then the height of the four filaments $\mathbf{H_{ideal}}$ = 0.2 +3 (0.4) = 1.4 mm. If we subtract the net change in the filament height, then $\mathbf{H_{actual}} = \mathbf{H_{ideal}} - \Delta\mathbf{H}$ = 1.3975 mm. To verify our result, we compare it with the measured value for the four printed layers from the previous experimental work (Ravoori et al., 2021), $\mathbf{H_{actual,ex}} = \mathbf{1.45}$ mm. the percentage error in our predicted value is equal to 3.76 %, which is an acceptable error. We can say that our model can predict the height of the 3D printed part with no ball rolling with acceptable accuracy. It is important here to point to the case with rolling that the expected theoretical filament height using our model is larger than the experimentally measured height. In the case of no rolling, the measured height value is higher than the theoretical value. The slight differences between experimental observations and our modeling results can be further minimized with additional considerations. For example, when modeling for the height of a 3D printed part with no rolling, it is crucial to count for the viscoelastic and swelling effect (Serdeczny et al., 2020). The swelling effect may lead to uneven filament height, poor filament adhesion, and even part warping, especially in large-scale printing (Serdeczny et al., 2020) (Brenken, 2017).

To include the swelling impact on our calculations, we have used a reported value from (Serdeczny et al., 2020), which give us the die-swell ratio $\mathbf{D_{sr}} = \mathbf{1.1}$ for PLA at 200°C printing temperature and at 60 mm/min feed rate (3600 mm/s printing speed) with 0.4 mm printing nozzle diameter.

The die-swell ratio is set to equal the filament maximum steady-state diameter $\mathbf{D_{max}}$ divided by the printing nozzle diameter $\mathbf{D_{nozzle}}$ (McIlroy & Olmsted, 2017). As such, for our case:

$$\mathbf{D_{sr}} = \frac{\mathbf{D_{max}}}{\mathbf{D_{nozzle}}} = \mathbf{1.1} \qquad (\mathbf{4})$$

Therefore, $\mathbf{D_{max}} = \mathbf{0.44}$ mm.

To verify this assumption, we will compare it with the previous experimental work (Ravoori et al., 2021). Let us assume that swelling was not initially present when the first layer was printed at a slow speed and low height. As such, the first filament height will remain fixed at 0.2 mm. The next filament's steady-state diameter, after we consider the swell effect, is equal to 0.44 mm. then the applied force, which is equal to the filament weight, equals $\mathbf{F = 0.00014\ N}$

For part one, we have the first filament diameter equals 0.2 mm and the second filament diameter equals 0.44 mm.

In the same way, we obtain the contact half-width value a = 8.74× $\mathbf{10^{-6}}$ m. Following the same procedure, for a = 0.00874 mm and R = 0.1 mm, we find h = 0.0996 mm and $\Delta\mathbf{H_1} = 0.00077$ mm.

For part two, we have the first filament diameter equals 0.44 mm and the second filament diameter equals 0.44 mm.

For this case, we obtain the contact half-width value a = 1.0892× $\mathbf{10^{-5}}$ m. In the same manner for a = 0.011 mm and R = 0.22, we find h = 0.2197 mm. and $\Delta\mathbf{H_2} = 0.0006$ mm. So, the final change in the height of the filament $\Delta\mathbf{H} = \Delta\mathbf{H_1} + \mathbf{3}\Delta\mathbf{H_2} = 0.0026$ mm.

The ideal height of the four filaments $\mathbf{H_{ideal}}$ = 0.2 +3 (0.44) = 1.52 mm, then $\mathbf{H}_{\mathbf{actual}} = \mathbf{H_{ideal}} - \Delta\mathbf{H}$ = 1.517 mm. To verify our result, we compare it with the measured value for the four printed layers from the previous experimental work (Ravoori et al., 2021), $\mathbf{H}_{\mathbf{actual,ex}} = \mathbf{1.45}$ mm. the percentage error in our predicted value is equal to 4.44 %, which is an acceptable error.

3.4 Results of case 4, lateral filament-filament contact

We need to study 3D printing parts' mesostructure; it is necessary to investigate the filament behavior in multiple directions. In this case, we examine two laterally (i.e., side by side) deposited PLA filaments' contact where no external load is applied. The contact half-width, in this case, will depend only on the traction between the two surfaces. Without any loss in generality, it can be assumed that printing begins with the deposition of the first filament deposited, then comes the second filament adjacent to the first one. We assume that the first filament temperature is equal to 90 ^{o}C and the second filament temperature is equal to 130 ^{o}C. As no external force is applied, and we don't know exactly how the contact area looks like, we use equation 31(Appendix A) instead of equation 28 (Appendix A). Our aim is to make an initial assessment of the value of the contact width for lateral contact the filaments.

Like before, we plot the nondimensional load $\widehat{\mathbf{P}}$ versus the nondimensional contact half-width $\hat{\mathbf{a}}$. Then, we read the $\hat{\mathbf{a}}$ value at $\widehat{\mathbf{P}} = \mathbf{0}$, which is $\hat{\mathbf{a}}$ = 2.48. Then by multiplying by $\mathbf{a_{IC}}$ = 2.25$\times$ $\mathbf{10^{-6}}$ m we can find $\mathbf{a = 5.58 \times 10^{-6}}$ m.

So, For a = 0.0056 mm and for R = 0.2 we find, which is in the lateral direction this time, h = 0.1999 mm. Therefore, the total change in the two filaments' width due to filaments interlocking equals 0.0002 mm, which we can consider a small value we can neglect. Appendix D summarizes all the results and parameters for each case of the previous cases.

Chapter 4

Meso-structure and Calculations of Void Fraction for Rolling and No Rolling Cases

4.1 mesostructure

One of the main goals of this paper is to find the effect of the ball rolling on the void fraction and compare it with no rolling. In our previous work, the void fraction was measured using "ImageJ" software (Ravoori et al., 2021). In the current research, we aim to use the previous results to calculate the void fraction. For the case of ball rolling, let us assume that we have two filaments initially both have the same radius before rolling i.e $R^{(1)} = R^{(2)} = 0.2$ mm. The two filaments have been subjected to two rolling passes. The first pass is over the first single filament, and the second pass is over the two filaments. As in section 3.2, we can solve for the filament height after the two rolling passes. For the first pass a = 0.071 mm and h = 0.187 mm. Therefore, the change in filament height equal $\Delta H_1 = 0.026$ mm. For the second pass a = 0.087 mm and h = 0.180 mm then, the change in filament height $\Delta H_2 = 0.039$ mm. Now, the net change in the height of the two filaments after two passes of the roller is equal to $\Delta H = \Delta H_1 + \Delta H_2 = 0.065$ mm. The final height of the two filaments, assuming the original height equal to 0.8 mm, 2H = 0.735 mm. To find the change in the height of a single filament, we can divide it by two, so the single filament height $H = 0.368$ mm. After two passes, the contact half-width equals the addition of the two previous values; therefore, the final contact half-width a = 0.158 mm.

We assume that as the filament is subjected to the load of ball weight or subjected to the load of

the upper filament weight, it will deform in such a way where the filament cross-section shape will change, but the area will remain conserved. In other words:

$$A_{\text{before loading}} = A_{\text{after loading}} \tag{5}$$

Assuming that the filament changes its cross-section shape from circular to elliptical like shape as suggested in figure 9, Therefore:

$$A_{\text{of circular cross-section}} = A_{\text{rectangel}} + 2A_{\text{circular sigment}} \tag{6}$$

$$\pi R^{(1)^2} = 2a \times 2h + 2\left(\frac{R^2}{2}(\theta - \sin\theta)\right) \tag{7}$$

But we also know for a circular segment:

$$H = 2h = R\sqrt{2 - 2\cos\theta} \tag{8}$$

We already know a, h, and $R^{(1)}$. So we have two equations with two unknowns, R and θ. Where R is the circular segment radius. And θ is the circular segment central angle. Solving, we obtain R = 1.557 mm.

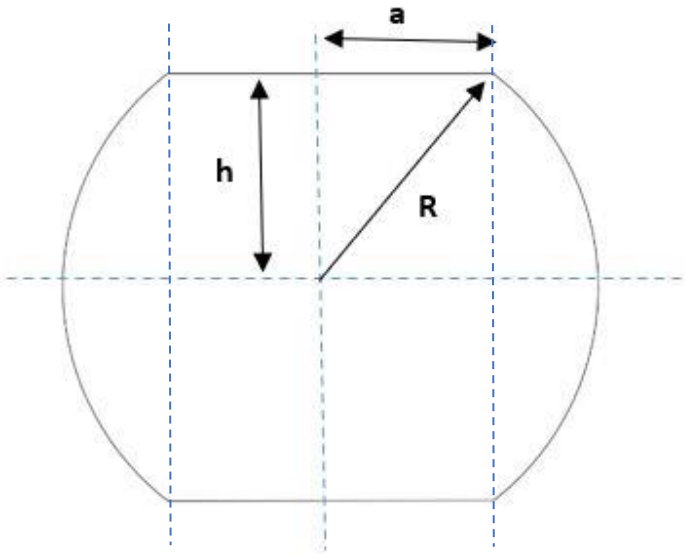

Figure 9: Schematic of predicted filament cross-section after applying load.

4.2 Void fraction

To find the void fraction, we draw four filaments cross sections by using the calculated geometrical values. Then,

$$\text{void fraction}\% = \frac{\text{Void Area}}{\text{Total Area}} \times 100\% \tag{9}$$

The total area for the four filaments is equal to the area of the four $2a \times H$ rectangles plus the area of the eight circular segments on left and right. Therefore.

$$\text{Total Area} = 4 \times (2a \times H) + 8 \times A_{\text{circular segment}} \tag{10}$$

So, the total area equals 0.5 mm^2. The void area is equal to two times the shaded area shown in the figure, which we can calculate by subtracting the area of two circular segments from the area of the green rectangle as shown in figure 22 (appendix E). Thus,

$$\text{Void Area} = 2 \times \left[(0.44 \times 0.023) - 2A_{\text{circular segment}}\right] \tag{11}$$

As such, the void area is equal to $0.0015 mm^2$. Consequently, the void fraction is equal to 0.3%.

For case 3 of figure 4, where the two filaments are in contact under the effect of the upper filament's weight, we assume that the filament changes its cross-section shape from circular to elliptical-like shape as suggested in figure 9.

Therefore:

$$\pi R^{(1)^2} = \pi R^2 + 2a \times 2R \tag{12}$$

Where $R^{(1)}$ is the filament radius before applying the load, and R is the filament radius after applying the load. For the case of no rolling with taking into account the swelling effect, the initial radius $R^{(1)} = 0.22$ mm and a = 0.011 mm solve equation 12 for R then R= 0.21 mm.

$$\text{void area} = (2R)^2 - \pi R^2 \tag{13}$$

$$\text{Total area} = 4 \times (2a \times 2R + \pi R^2) \quad (14)$$

We find the void area and total area equal to 0.038 mm^2 and to 0.5 mm^2, respectively. Then, the void fraction is equal to 6.3%. Our void fraction calculation for the case with no die-swell effect gives the same void fraction for both cases, i.e., with swell effect and without swell effect.

4.3 Results of the mathematical model

Table 1 shows the four configurations to compare with the measured void fraction. The table also shows the reduction in the layer height. It appears that the void fraction we calculate by using our model differs slightly from the measured value. We believe that the printing and rolling process for polymers involves several chemical and physical processes. We model the rolling at the instant when the ball passes over an area of interest because most of the significant microstructural changes on the part and the filament cross-section occur when the filament is still soft and deformable. It should be noted that some other factors like printing speed, rolling speed, friction, and viscoelasticity effect are not included in this model for simplicity.

Table 1: Comparison of geometrical parameters between actual and predicted mesostructure.

	Description	Height of four filaments (mm)	Reduction in filament height%	Void fraction %	The error of predicted height%
Model	No ball rolling (no swell effect)	1.3975	8.5%	6.3%	3.76%
	No ball rolling (with swell effect)	1.5174	15.7%	6.3%	4.44%
	With ball rolling	1.2790	-	0.3%	5.39%
Experiment	No ball rolling	1.4500	16%	10.3%	-
	With ball rolling	1.2100	-	0.7%	

4.5 Results of adhesion and pull-off force

Our study is mainly about the effect of the change on surface energy due to elevated temperature on the PLA filament behavior under specific printing and rolling considerations. Polymers adhesion with other materials and with themselves, subjected to multiple mechanisms. Many theories are available to describe polymer bonding and adhesion behavior. The current study is limited to examining how PLA surface energy changes affect the PLA-PLA and PLA-steel adhesion. Adhesion due to change in surface energy can be investigated by studying the pull-off force. Rewriting equation 28 (Appendix A) in the form as in equation 31 (Appendix A) will allow us to examine the effect of temperature change on the pull-off force.

To study the pull-off force over a range of temperatures, we plot M_2 versus $\widehat{P}_c$ for both the steel ball-PLA filament contact and the PLA-PLA filaments contact. For both cases, the maximum pull-off force occurs at a contact state just higher than isothermal with M_2 slightly more than 0. For our contact conditions, the contact is a little lower than isothermal contact where $M_2 = -0.03$ and -0.1 for steel-PLA contact and PLA-PLA contact, respectively. Also, we find $\widehat{P}_c = 1.005$ for Steel-PLA contact and $\widehat{P}_c = 0.992$ for PLA-PLA contact.

4.6 Conclusion

3D printing parts by using the FFF technique involves layer-by-layer deposition of soft and heated filaments. As illustrated in Fig. 21 or 22, the resulting structure always contains some percentages of voids. This study suggests that applying pressure by rolling immediately after depositing decreases the void fraction significantly. The study also shows that rolling can provide good control over the part thickness, reduce the effect of die-swelling, and prevent poor adhesion and part warping. Applying pressure on soft filaments results in reshaping the filament cross-section

to look more like an elliptical shape. This new shape has longer contact width, which gives more area for polymer chain diffusion and thus higher interlaminar strength.

Our model predicts the printed part height for rolling with 5.39% error and no rolling with 4.44% error. Through this finding, the final height of the printed structures could be predicted. This study also gives a future recommendation for a new configuration of preheating and post-rolling, which further improves the interlaminar 3d printed parts strength. This chapter shows that the JKR contact theory, along with the theory of elasticity, can be used to predict the final height of 3d printed parts along with their mesostructure.

Chapter 5

Fracture Behavior of Rolled and Baseline 3d Printed Parts

5.1 Introduction

Studying crack propagation which causes failure in engineering materials, is called fracture mechanics. Fracture toughness, or material resistance to fracture, is an essential material property in fracture mechanics. It characterizes the material behavior with the presence of cracks in the material structure. Strain energy release rate or fracture energy measures the required energy for the crack to propagate and create new surfaces along the crack tip. The two main types of fractures are brittle fracture and ductile fracture. In brittle fracture, the fracture happens suddenly and catastrophically with little energy absorption. In ductile fracture, the material yields before fracture. The fracture toughness of engineering materials and fracture propagation behavior can be influenced by temperature, strain rate, and stress state. Some materials are more ductile under higher temperature conditions and lower strain rate loading and as the stress state goes from tri-axial to bi-axial to uni-axial. A crack is a sharp void, hole, or discontinuity in the material structure, amplifying stress concentration. Linear elastic fracture mechanics (LEFM) was one of the earliest fracture theories. LEFM concerns mainly the brittle fracture where the crack is sharp, and the crack propagation is sudden. Crack can propagate under three modes of loading; mode I or the opening mode, mode II or the sliding mode and mode III or the tearing mode. The crack could be under

mixed-mode loading, combining two or three of the previous mods. Fracture mechanics analysis can be performed under different scaler levels: atomic, microscopic, and continuum. In the current research, the study will be on the continuum level where the material has been assumed to behave isotopically. (Anderson, 2005).

The fracture behavior of 3d printed parts depends on many factors such as printing temperature, printing speed, layer thickness, and filament-filament contact width(Ahmed & Susmel, 2017). As we have mentioned earlier, interlayer strength is one of the most critical weaknesses of 3d printed parts, especially in applications where loading is in a transverse direction with the printed filaments (Fonseca et al., 2019). (Coogan & Kazmer, 2017) found that increasing printing speed, nozzle temperature, and filament width results in increasing filament-filament bond strength, and increasing layer height results in weakening the bond, while printing bed temperature doesn't have a significant influence. Another research paper (Noori, 2019) found that printing layer height, in a range between 0.2 – 0.4, mm doesn't considerably affect interlayer fracture energy for 3d printed PLA material.

Fracture energy, in terms of strain energy release rate G_{IC}, for PLA thermoplastic material, reported in the literature with a range varies according to material processing. 19 $\frac{kJ}{m^2}$ for neat pla (Pérez et al., 2018), 5 - 30 $\frac{kJ}{m^2}$ for drawn PLA plates with drawing ratio rangs from 1 to 2.5 and, 16, 13 $\frac{kJ}{m^2}$ for unannealed and annealed 3d printed pla, respectively. So, as it is noteworthy that production processes can affect PLA fracture behavior significantly, We intend to investigate the effect of rolling after printing on the fracture behavior and the interlayer strength for 3d printed PLA. We also propose to study the impact of the pressure that comes from printing with lower

layer height versus the effect of pressure load that comes from rolling after the printing process on 3d printed part's fracture properties. The other aim is to find a relation between the filament-filament contact width and the part fracture behavior. We build a FEM model using the Ansys workbench to find the stress intensity factor at different contact widths. Finally, we carry out experiments at different environmental temperatures to see how it will affect part cracking.

5.2 Experimental investigation of the effect of rolling after printing on part fracture behavior

In our study, we are interested in investigating the effect of rolling after printing on the inter-laminar strength of the printed/rolled part. We found that the contact width between the filaments increased when we used the rolling after printing technique. We expect that the interlaminar fracture strength and toughness have improved as well.

To investigate the effect of rolling-after-printing, we design a 3 point bending fracture test over a v-notched sample by following the sample dimension as suggested by (ASTM D5045 - 14) standard for testing plastic materials and similar to (Hart & Wetzel, 2017). This test aims to measure mode one or opening mode fracture strength of both the rolled and baseline samples, as shown in figure 10.

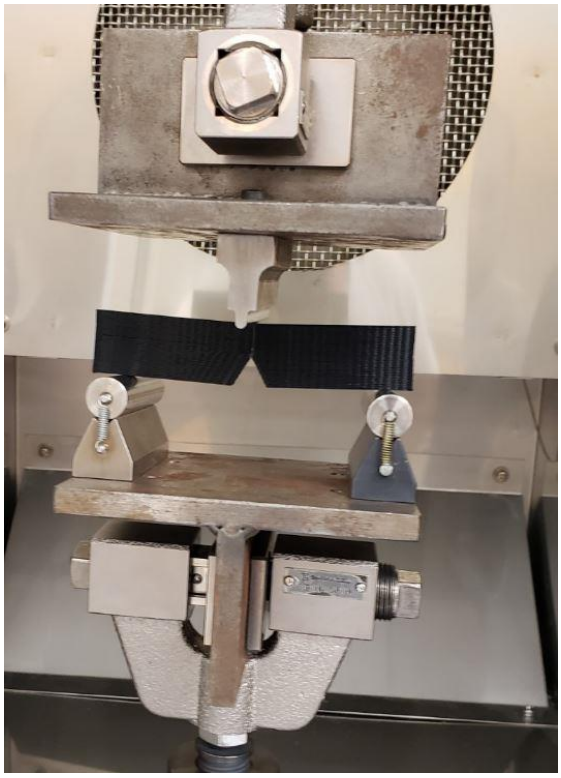

Figure 10: Illustration for experimental setup for 3 point bending test applied over a v-notched angle.

We use a v-notched sample with a notch angle equals to 53.13^{o} as shown in figure 11. The v-notch helps avoid some common printing/rolling complications and design limitations where we need the rollers to pass over the part orderly and equally to prevent excessive heating.

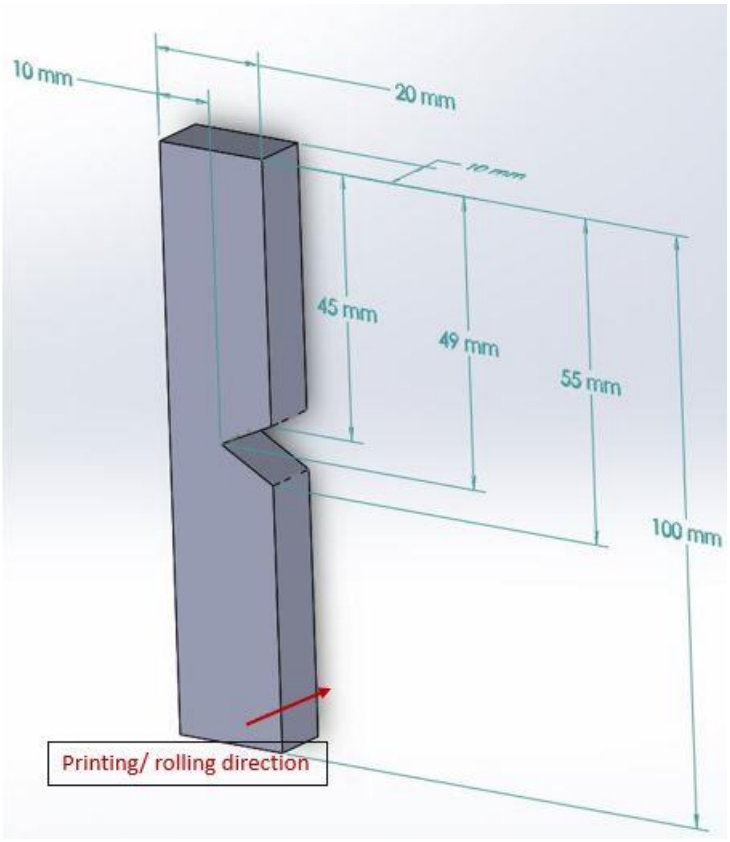

Figure 11: Illustration of 3D printed v-notch sample for 3 points bending fracture sample.

We print two kinds of specimens (baseline and rolled) with 3600 mm/min printing speed and with 0.37 mm filament height using an open-source Anet A8 3D printer. The printing temperature equals 200 ℃, the rolling ball temperature equals 110 ℃ the printing/rolling direction has a 90-degree angle with the loading direction along the short part's edge, as shown in figure 11. We use dual-sided rolling after printing technique, and we follow the optimal printing/rolling parameters as described in our previous work (Ravoori et al., 2021).

We conduct a fracture test by using Shimadzu AGS-X series universal test machine with a high precision 5kN load cell and a load rate of 1 mm/min. We conduct the test until the complete

fracture. We use the recoded force and displacement along the test to plot the load-displacement curve. The fracture test results show that the maximum load for rolled part (554.5 N) equals about 1.85 times the maximum load for the baseline part (299.8 N), as shown in figure 12.

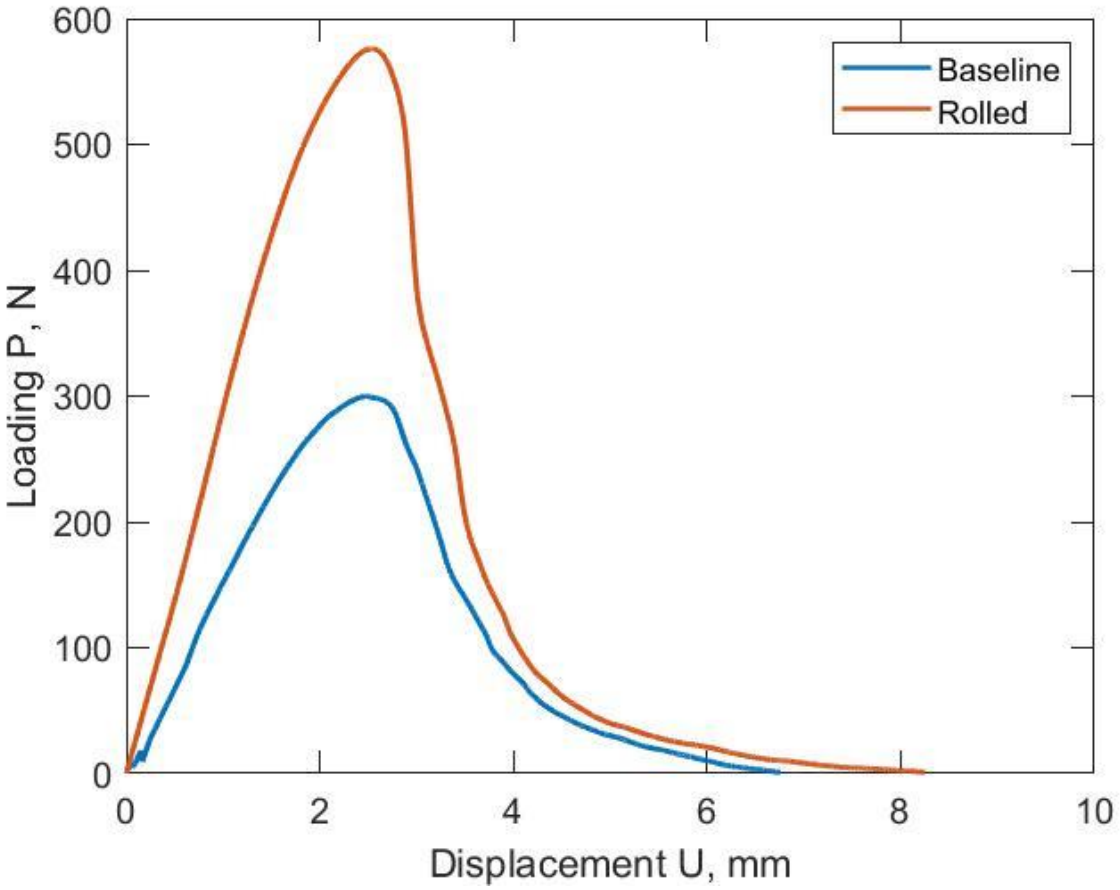

Figure 12: Load-displacement curve for 3 points bending fracture test for rolled and baseline samples.

Another kind of printed part has been tested similarly. This third kind of part was offered by Raised3D Technologies company and printed using a high-quality 3d printer. The part's dimensions are very precise, and the surfaces are very smooth. The printing layer height equals

0.24 mm, and all other printing parameters are the same as the baseline parts. The aim of adding this kind of part is to probe the effect of printing layer height and the effect of printer quality versus the rolling effect. As shown in figure 13, the comparison results reveal that the third part has almost the same printing strength as our baseline sample with the behavior of progressive fracture.

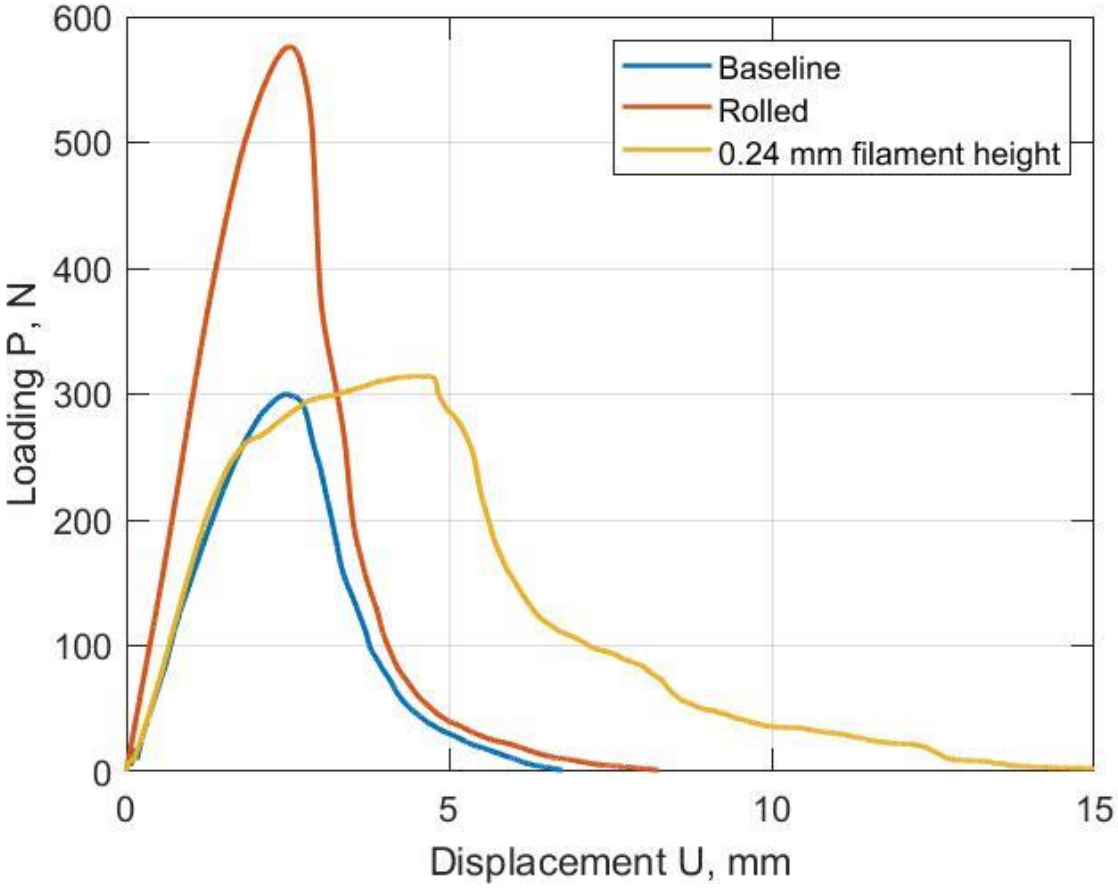

Figure 13: Load-displacement curve for 3 points bending fracture tests including the 0.24 mm layer height sample

By looking at the part's fracture surface and the displacement-load curve, we have noticed that the third kind of parts failure was a gradual fracture with crack propagating laterally between the printed filaments at the crack initiation, as illustrated in figure 14. This fracture means that the third kind part has less interlayer bonding. This result emphasizes that the rolling effect results in reducing parts height and improving filaments interlayer bonding and, therefore, enhancing the part fracture properties. Also, we ensure that the pressure from ball rollers has a different effect on the part's fracture properties from the pressure from the printing nozzle due to printing with lower layer height.

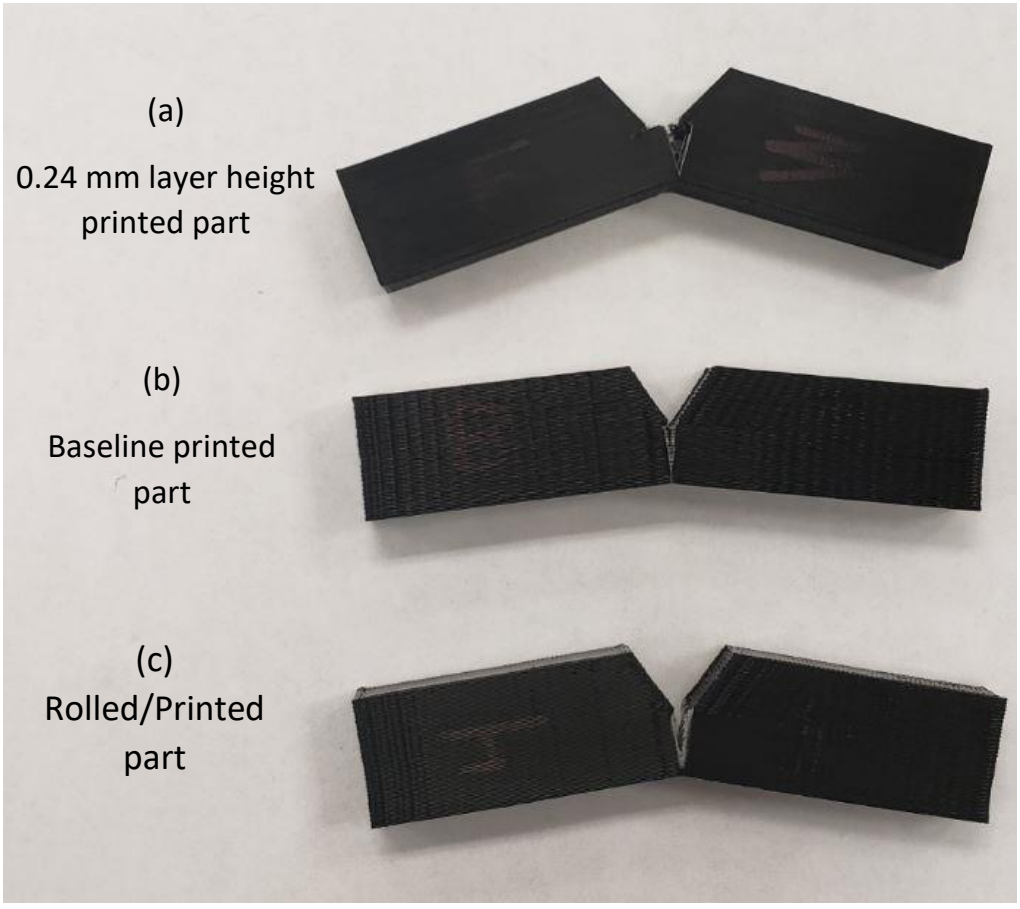

Figure 14: Fracture surface and propagation line for (a) 0.24 mm layer height part. (b) Baseline printed part. (c) Rolled/printed part.

If we look at part's fracture surfaces, we can notice that the overall fracture behavior for the three parts is a brittle fracture. We also see crazing fracture behavior on the rolled specimen, as shown in figure 14. The white lightening around the fracture line can be noticed for the rolled sample. This result provides evidence that the material fracture properties have improved by the rolling-after-printing technique.

Crack initiation load, or critical load P_{Cr} has a significant effect on the pre-cracked part's fracture behavior. The point on the load-displacement curve where the behavior starts changes from linear to nonlinear is associate with the start of crack propagation and the critical load (Aliheidari et al., 2017). As we have mentioned previously that the level of our study is continuum scale, so our findings for the critical load have been recorded by observing the instant of crack initiation by the unaided eye. Then we try to match the recorded values for the critical load with the point on the load-displacement curve where the behavior starts transferring from linear to non-linear after a small sort of yielding. To find this point, we zoom in on the very beginning of the load-displacement curve, as shown in figure 15. We believe that more experiments may be needed to observe the instant of crack initiation more precisely by using a high-quality camera where the crack can be observed on the microscopic level.

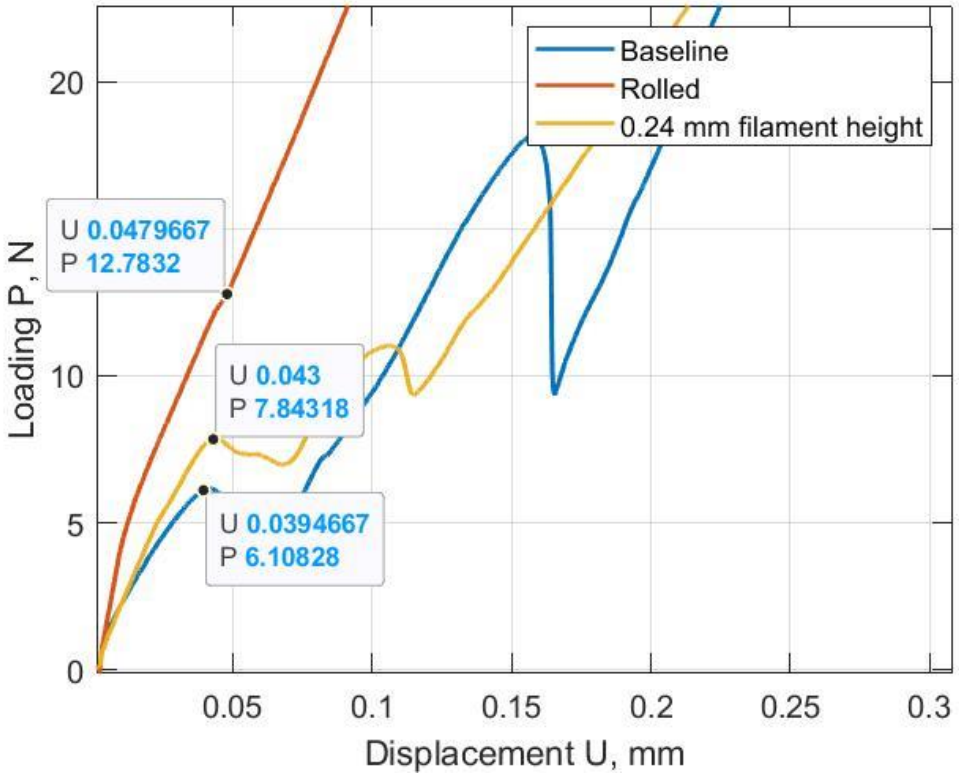

Figure 15: Illustration for crack initiation loads for Baseline, rolled, and 0.24 mm layer height 3D printed parts.

The critical load P_{Cr} values can be used to find the critical stress intensity factor K_{IC} and the critical strain energy release rate G_{IC} by using equation 15 and equation 16. Values for P_{Cr}, K_{IC}, G_{IC} are summarized in table 2. It is crucial to mention that equation 15 is used mainly for single notched 3 points bending fracture sample with a notch angle equal to zero. In our case and according to (Leguillon et al., 2007), changing the notch angle from 0^o to around 60^o dosent have a significant effect on the measurement of stress intensity factor. So we assume that equation 15 can be used for finding the stress intensity factor for our v-notched sample with acceptable error.

$$K_I = \frac{PS}{BW^{\frac{3}{2}}}\left[2.9\left(\frac{a}{W}\right)^{\frac{1}{2}} - 4.6\left(\frac{a}{W}\right)^{\frac{3}{2}} + 21.8\left(\frac{a}{W}\right)^{\frac{5}{2}} - 37.6\left(\frac{a}{W}\right)^{\frac{7}{2}} + 38.7\left(\frac{a}{W}\right)^{\frac{9}{2}}\right] \qquad (15)$$

The equation parameters are illustrated in the following figure.

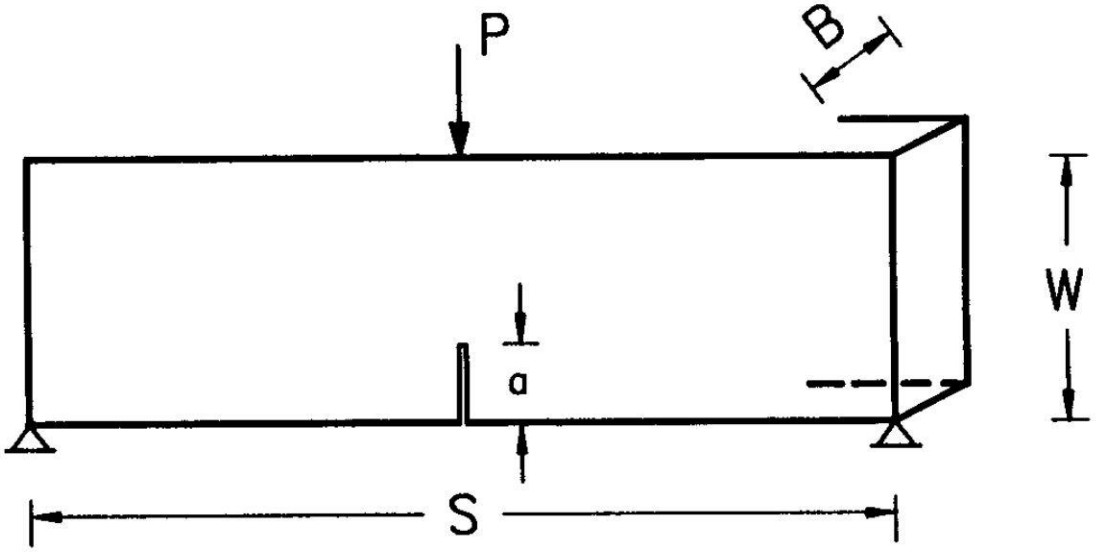

Figure 16: Schematic illustration for 3 points bending test's loading and geometrical parameters for a pre-cracked sample.

As we have a pre-cracked sample, the load where the crack starts propagating is equal to the critical load, and at that load, the crack will be considered a critical crack. By substituting both values in equation 15, the calculated stress intensity factor will be deemed critical and equal to K_{IC}. Now, we can use this K_{IC} value to find the critical strain energy release rate by using equation 16 for the plane strain case.

$$G_{Ic} = \frac{\mathrm{K_{Ic}}^2(1-\nu^2)}{\mathrm{E}} \tag{16}$$

It is important to point here for the modulus of elasticity E, where it is recommended to measure E with the same condition as in the v-notched sample (ASTM D5045 - 14). Our previous research paper (Ravoori et al., 2021) plotted the stress-strain behavior for both the baseline and the rolled samples. By using this plot, we find E for both kinds of pieces to be equal to $E_{rolled} = 874.5\ MPa$ and $E_{baseline} = 472.9\ MPa$ as illustrated in fiugure 17. E for the third kind of parts (Raised3D's

part) is not available so we couldn't find it's G_{IC} value.

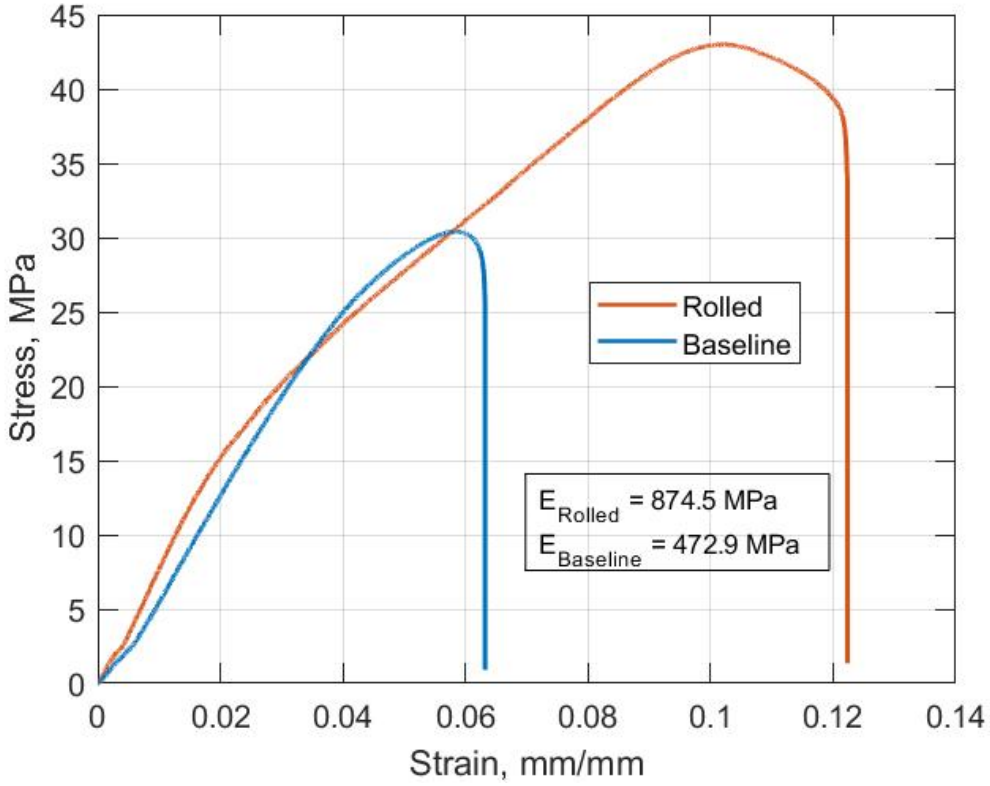

Figure 17: Stress-Strain curve for tensile testing of baseline and rolled 3D printed parts to find the part's modulus of elasticity.

The critical stress intensity factor is a material property that depends on the part geometry (decreasing as the part's thickness increasing) in contrast to the critical energy release rate. In the literature for PLA $G_{IC} \approx$ 19.3 KJ/m^2 (Pérez et al., 2018). This value comes in between our measured values for rolled and baseline samples. To validate our critical load measurements, we run a FE study by using the Virtual Crack Closure Technique (VCCT) to find the critical load that is corresponding to the critical fracture energy G_{IC}. We find that a load of 10 N over a 3 point bendind test sample will consider critical for a bulk PLA material and and results in G_{IC} =19.28 KJ/m^2. We think this range for G_{IC} is due to the wide range in PLA modulus of elasticity 0.05-

13.8 GPa which affected by several parameters such as production processing. Heat treatments can also affect PLA fracture energy (Gámez-Pérez et al., 2011). In our case, hot rolling provides some extra heat after printing, which instantly changes the part's cooling rate and results in better fracture properties similar to pre-and-post heating (Ravoori et al., 2019b). It is crucial to invoke that the critical values for all fracture properties are considered critical only for our specific part's dimensions.

Table 2: Summary for measured and calculated fracture test critical results.

Printed part	Max strength, P_{max} (N)	Crack initiation load, P_{Cr} (N)	Critical stress intensity factor SIF, K_{IC} (MPa.$\sqrt{mm}$)	Critical Strain energy release rate, G_{IC} (KJ/m^2)
Rolled/Printed	565.04 ± 10.55	12.41 ± 0.37	183.75	33.6
Baseline/Printed	294.26 ± 5.54	6.22 ± 0.13	69.54	8.89
0.24 mm fil. height	306.40 ± 7.47	7.05 ± 0.79	78.82	
Bulk PLA		10 (VCCT FE Model)		19.3 (Pérez et al., 2018)

From our measurements, it is clear that all fracture parameters have improved significantly for rolled parts compared to the baseline parts. We believe that enhancing adhesion between the printed filaments due to applying compression load acts and reshaping the deposited filaments to have longer contact width result in a part with 277% higher filament-filament fracture energy under model I loading type. Additionally, we think that rolling the filaments results in improving the PLA

filament’s fracture properties along the rolling direction, resulting from reorienting polymeric molecules similar to the effect of PLA plate drawing (Todo, 2007). On the other hand, the 3D printed part with 0.24 mm layer height shows a slight improvement (13%) in both the critical crack initiation load and the critical stress intensity factor. We think that the effect of rolling pressure outperformed the effect of nozzle pressure which comes from printing with lower layer height. Moreover, even though printing with lower layer height provides more contact area between the two printed layers, it doesn’t improve the fracture toughness in a considerable amount. While increasing the filament-filament contact area proves that it is an essential factor in improving 3d printed part’s fracture behavior. In the next section, we intend to study the effect of filament-filament contact width on the part's fracture properties and find the contact width impact on the rolled part’s fracture parameters.

5.3 Effect of contact width on the fracture behavior of 3d printed parts

In the literature, (Rezaee & Adnan 2018b) conducted a study on the elastic stress singularities and mode I notch stress intensity factor (SIF) for 3D printed polymers. The study took into account the singularities created when the fused filament fabrication was used (FFF). The FFF method extrudes the material layer by layer, which leads to partial healing and stress singularity points between the material layers. They found that the FFF parts' fracture properties can be improved by increasing the negative gap setting and the notch angle. Chapter four shows that the notch angle has increased at the interface between the rolled filaments. Also, The results show that the rolled filaments have a longer contact width, which means lower singularity order and better fracture properties. This observation encourages us to work on a finite element study that relates the filament's contact width with the fracture properties of the printed rolled and baseline parts.

Throughout this study, we have proved the importance of the filament-filament contact width and the filament shape on the part's mechanical behavior. To further emphasize our findings, we build a FEM model to investigate the effect of the filament shape and the contact width of two filaments in contact on the fracture properties. This study will give clearer sight of the impact of the rolling-after-printing technique. We create a v-notched fracture test sample that represents two printed filaments in contact. This model will simulate a fracture test on a v-notched piece.

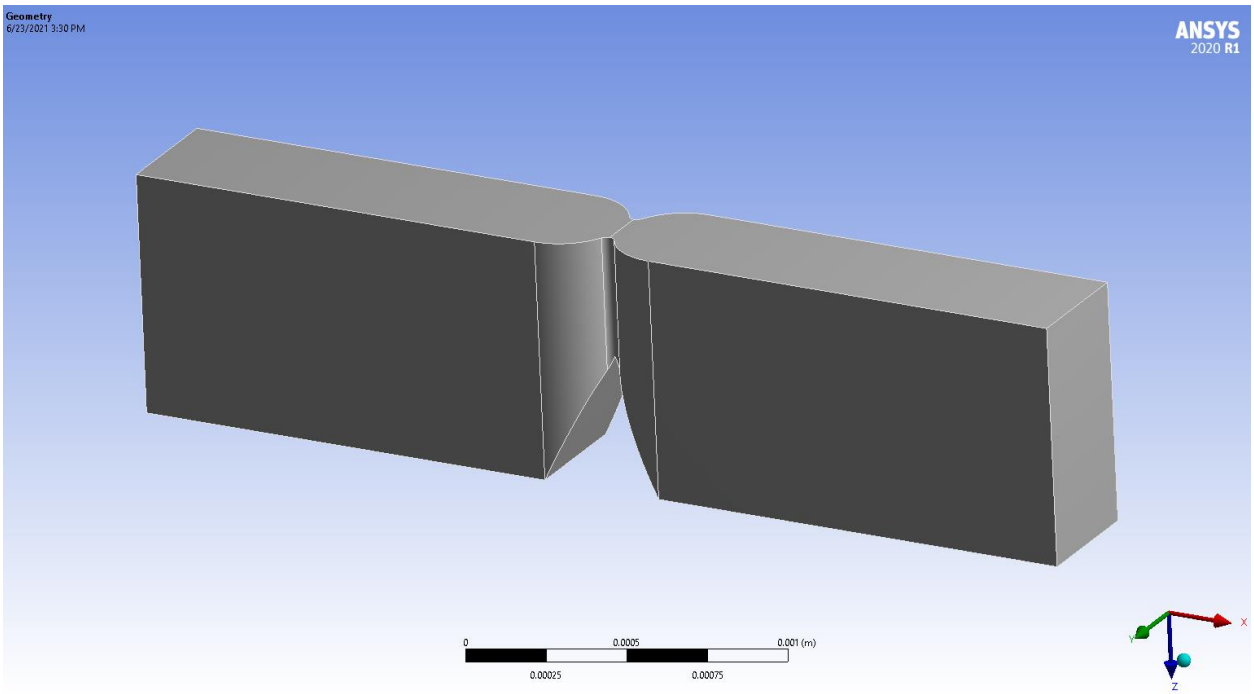

Figure 18: Schematic for the part used in the FE model.

Ansys workbench has been used to build our FEM model. SMART crack propagation is a new powerful tool to study fracture and crack propagation behavior through FEA. SMART stands

for Separating Morphing and Adaptive Remshing Technology. SMART propagation tool adopted the unstructured mesh method (UMM), allowing for regenerating mesh around the crack tip and reducing the required computational load. (Ayhan, 2011) explains the use of UMM in finding SIF. The required element type in this method is Tetrahedron. We use a spherical mesh control to create a smaller mesh around the crack tip to reduce the computational load further. The pre-meshed crack type has been used along with the SMART crack propagation technique. The result of this simulation is the stress intensity factor along with crack propagation.

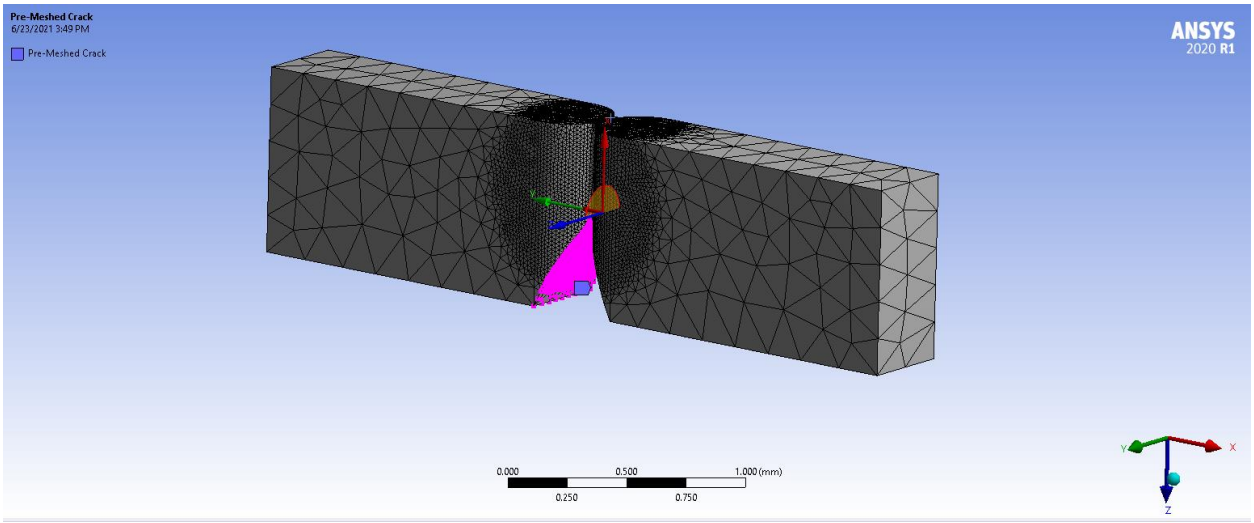

Figure 19: Illustration for the mesh and the pre-meshed crack used in the FE model

Simply supported part with displacement load along the edge, as shown in figure 20, has been used in our model. we have used displacement type load to reduce the singularity due to a line load over part's edge. Also, we want to study the effect of the contact width by applying the same test conditions over different contact widths and contact angles. For each geometrical configuration, a particular force load is required to initiate crack propagation. To avoid these complications, we use displacement load.

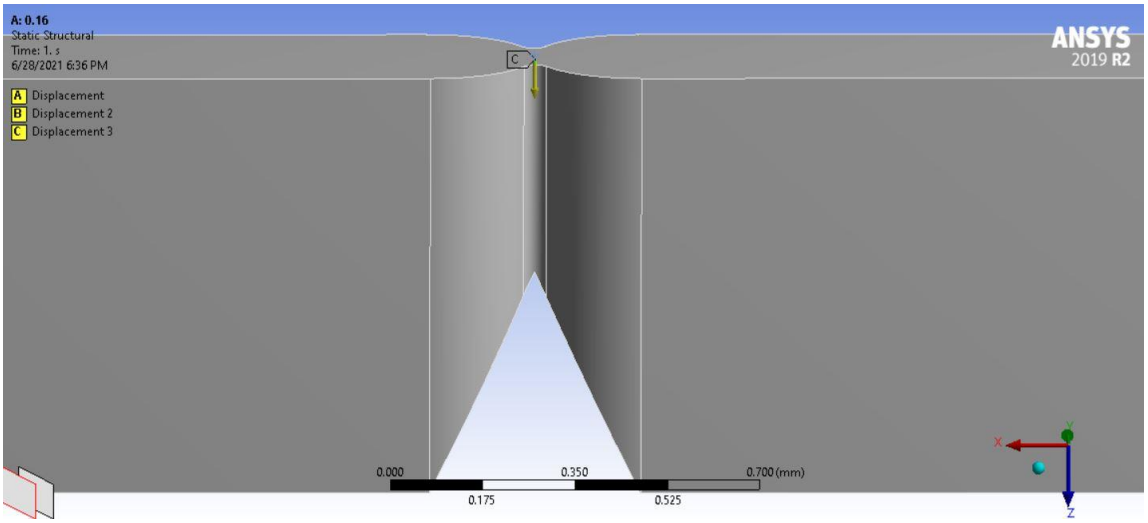

Figure 20: Loading configuration for the FE model

After applying the load, the crack starts propagating until it reaches the maximum deflection, as illustrated in figure 21. The fracture propagation line and the fracture surface are pretty similar to the experimental results. The crack propagates between the two filaments; this allows us to find mode I stress intensity factor K_I along the contact area. This K_I represents the interlaminar stress intensity factor that we intend to find.

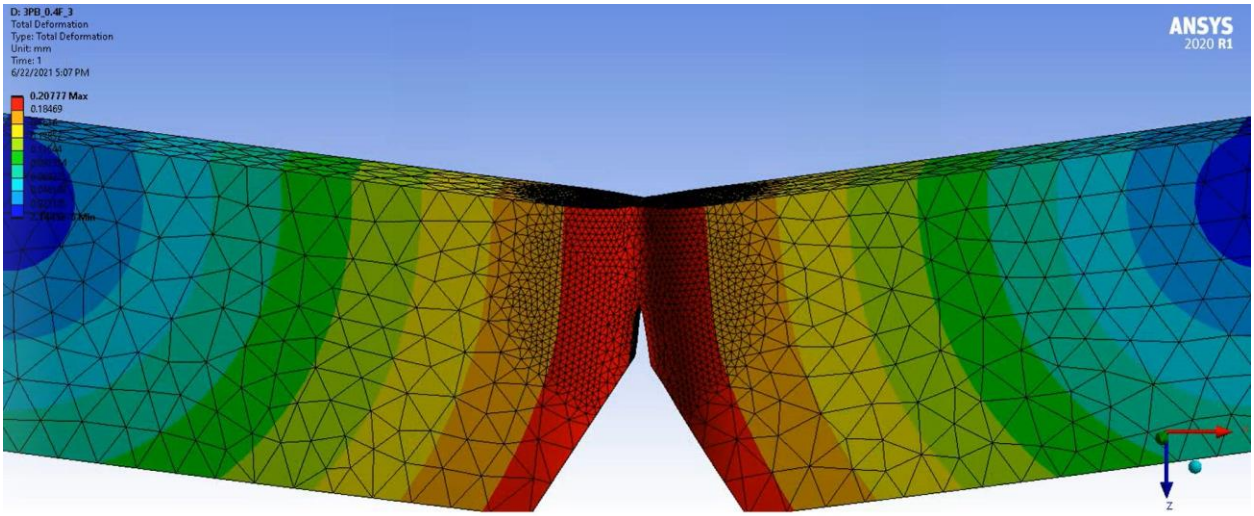

Figure 21: Illustration for the part deflection and the crack propagation.

As expected, the SIF increases with increasing the crack length and reaches its maximum value at the end of crack propagation. It is necessary to mention here that the value we find in this simulation is the stress intensity factor K_I not the critical stress intensity factor K_{Ic}. Where K_I is a variable value that depends on the load, crack length, part geometry, and material. While K_{Ic} is a material property that is equal to K_I when the crack is about to start to propagate.

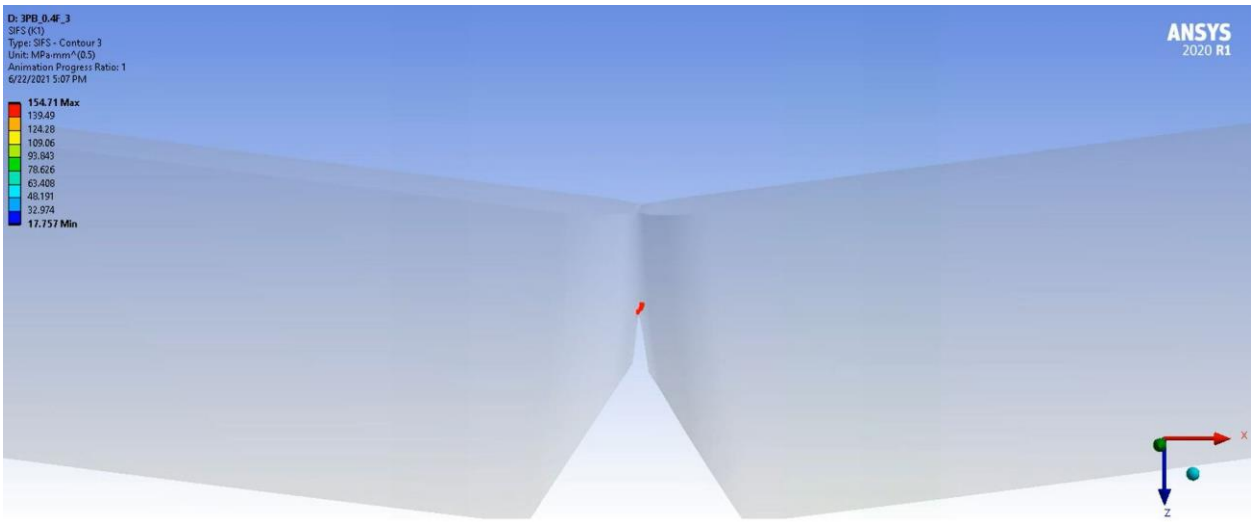

Figure 22: The result of SIF at the end of the simulation test.

We accomplish a mesh refinement study to ensure solution convergence. We create a finer mesh size around the crack tip, and we make sure that reducing the mesh size results in converging the stress intensity factor to a certain value, as shown in figure 23.

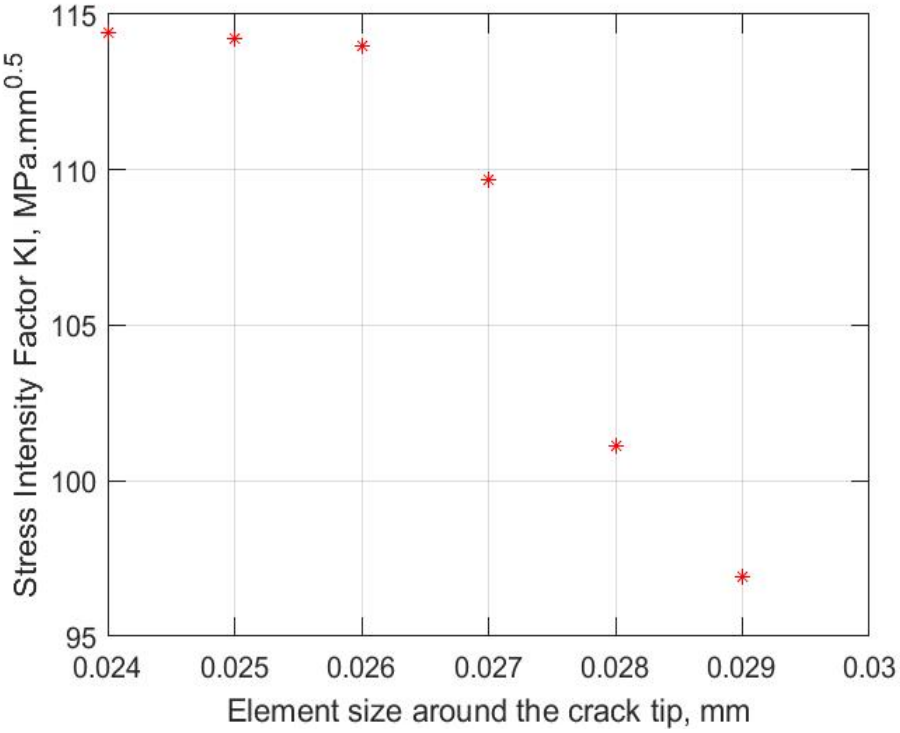

Figure 23: Results of mesh refinement study.

Our next step is to create a model to study the effect of contact width versus the part width on the part's mode I stress intensity factor K_I. As represented in figure 24, we have two models. In model 1, the change happens in the part's contact width (2a), which appears as necking between the two filaments in contact. In model 2, we change only the part thickness (2x) to compare the effect of changing 2a versus 2x.

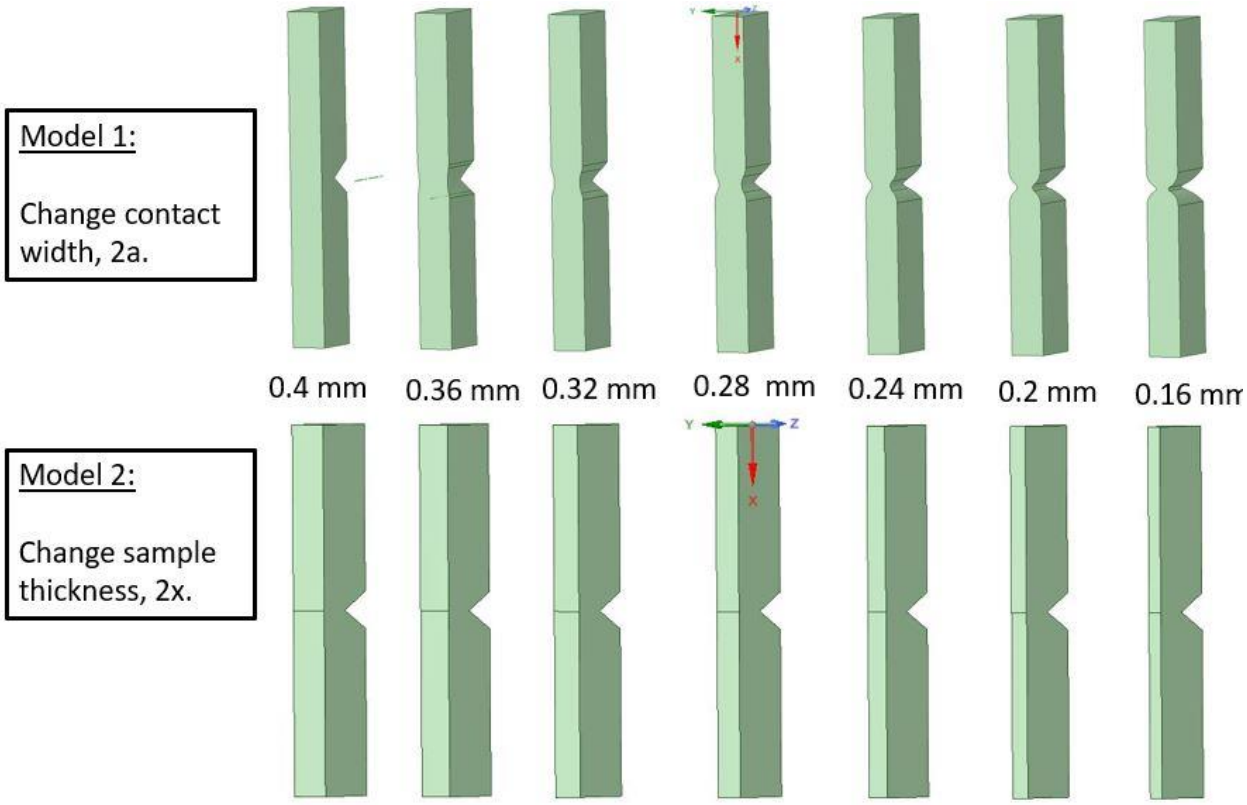

Figure 24: Models used to find the effect of the contact width 2a and the effect of part thickness 2x on the part's fracture behavior.

We use the same procedure as in the last section to plot the result of SIF K_I over different contact widths as in figure 25. We use these results to find a mathematical relation between the contact width 2a and the stress intensity factor K_I. By using curve fitting, we plot and extract an equation to relate 2a to K_I.

$$K_I = -20.16 \times 10^6 + \frac{179.73 - -20.16 \times 10^6}{1 + \left(\frac{2a}{402.96}\right)^{1.78}} \quad (17)$$

We take advantage of this mathematical relation to find and compare the stress intensity factor K_I for the rolled and baseline samples. We use the results from chapter four ($2a_{rolled} =$

0.316 mm, $2a_{baseline} = 0.022\ mm$) and substitute numbers in equation 17. we find $K_{I,rolled} = 119.38\ MPa.mm^{0.5}$ and $K_{I,baseline} = 179.21\ MPa.mm^{0.5}$. These values for SIF means that at the same loading and geometrical conditions, SIF is 40% less for rolled parts in comparison to baseline, which means higher critical load P_{Cr}, higher critical SIF K_{Ic} and indeed better fracture properties. If we compare the SIF for the rolled and the baseline samples with the case of 2a = 0.4 mm, which has no necking between the two filaments (bulk material). We find that $\frac{K_{I,rolled}}{K_{I,bulk}} = 1.36, and\ \frac{K_{I,baseline}}{K_{I,bulk}} = 2.04$. which means rolling-after-printing makes the 3D printed part's fracture behavior closer to the bulk material part's fracture behavior.

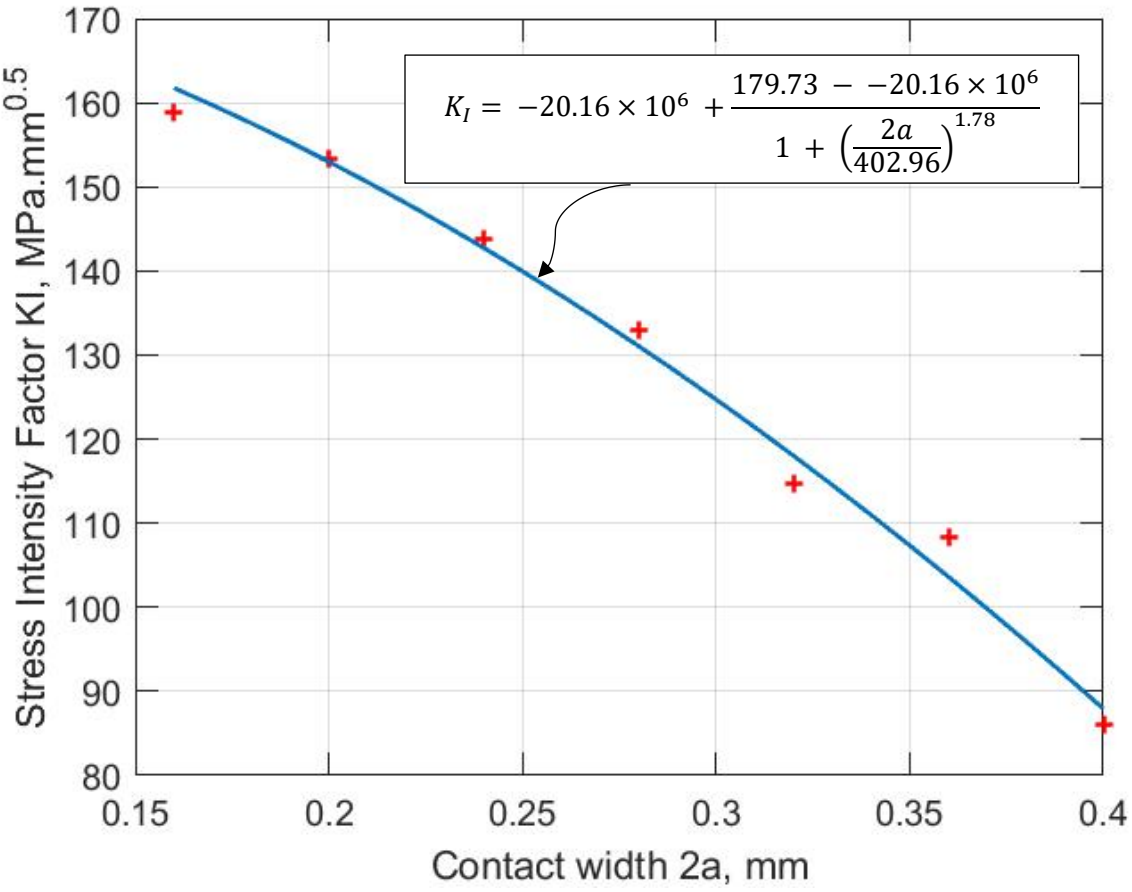

Figure 25: Result of FE model and the curve fitting for the SIF versus contact width 2a.

The question that appears now is, is it only the contact width effect that affects the SIF? To answer this question, we created model 2, where we study the impact of change only the part thickness 2x. The result for this model shows in figure 26.

By using the same method, we find the relation between the SIF and the part thickness. It is clear from figure 27 that it is not only the effect of changing the part thickness or the contact width. Other factors play an essential role in 3d printed part's fracture behavior, such as the angle between the two filaments (Rezaee & Adnan, 2018a).

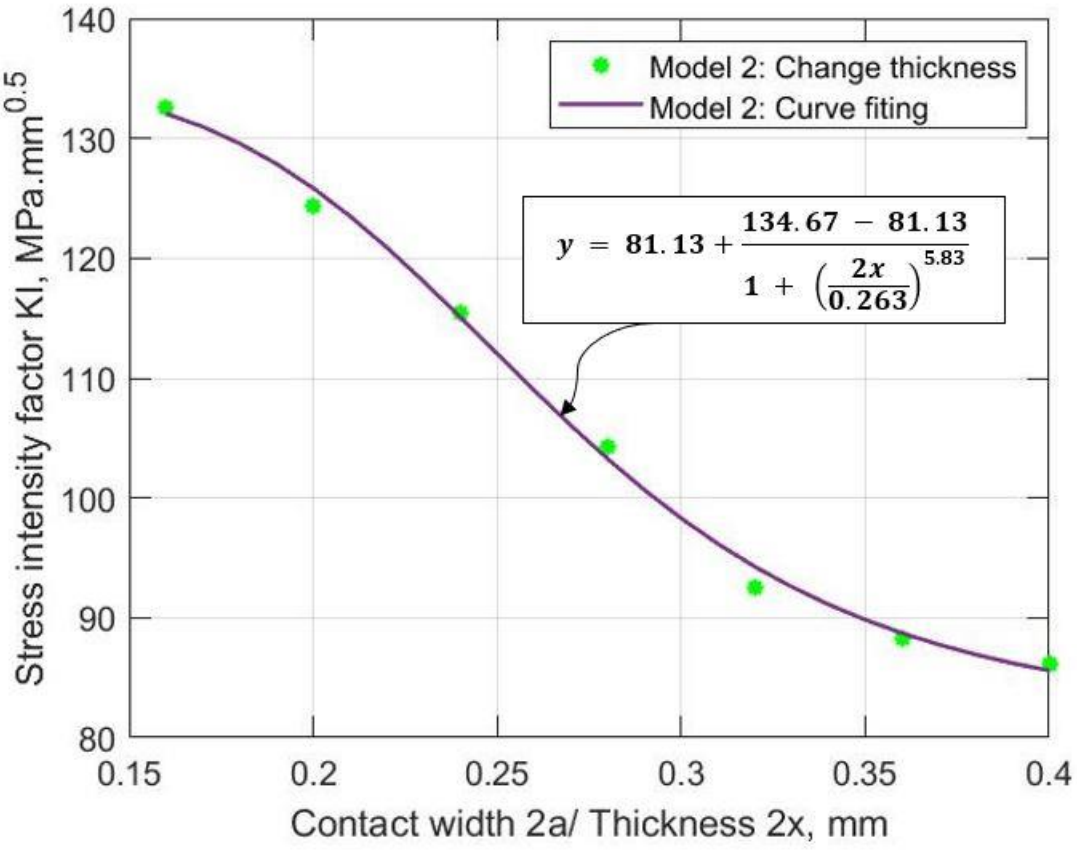

Figure 26: Result of SIF as a function of the part's thickness for the FE study and curve-fitting relation.

Figure 26 shows the relation between the stress intensity factor and the part thickness, which can be stated as in equation 18 by using curve-fitting.

$$y = 81.13 + \frac{134.67 - 81.13}{1 + \left(\frac{2x}{0.263}\right)^{5.83}} \quad (18)$$

If we plot the two curves on the same sheet as in figure 27, we can notice the difference between the values and the trend of the curves of the two models. Let us apply the rolled and baseline contact width on both models. We find that $\frac{K_{I,rolled,Model1}}{K_{I,rolled,Model2}} = 1.26, and\ \frac{K_{I,baseline,Model1}}{K_{I,baseline,Model2}} =$ 1.33. these results ensure the importance of including the contact width and the contact angle between the filaments as factors that affect the part's fracture behavior.

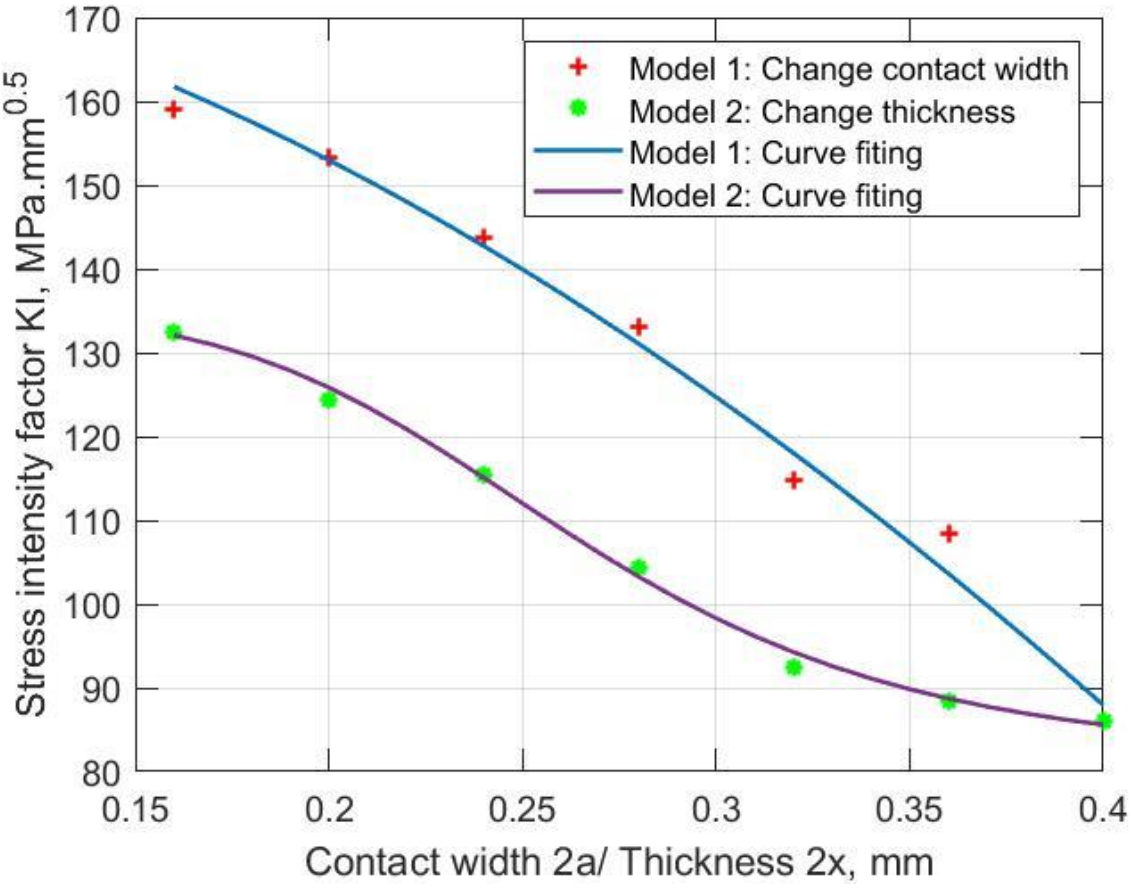

Figure 27: Comparison between the effect of the part's contact width 2a and the part's thickness 2x on the stress intensity factor SIF,

Up to this point of our research, we studied the behavior of the printed parts under several circumferences. Still, as we are dealing with thermoplastic material, testing the material at different temperatures will add considerable knowledge to the part's behavior. In the next section, we sought to study the fracture behavior of rolled 3d printed parts under a range of operating temperatures.

5.4 Effect of environmental temperature on the fracture behavior of 3d printed parts

We design an experiment to investigate the fracture behavior of 3d printed filaments when the working environment is higher than and lower than the room temperature. Such a study will help

to understand the fracture behavior of some industrial applications where 3d printed parts can be used, such as 3d printed heat exchangers and 3d printed electronic devices.

An illustration for the experiment is shown in figure 10, where we have a v-notched printed sample tested inside a temperature-controlled heat chamber similar to section 2.4. The test is a 3 point bending test. The parts are printed/rolled in a way where the v-notch is facing up. Other printing and testing parameters are the same as in section 5.2.

For parts tested at 35℃ and 45℃, the heating chamber maintains at 37℃ and 47℃, respectively to overcome heating losses. For parts tested at 0℃ and 4℃, we put them in a fridge and freezer, respectively, for around 3 hours and then tested immediately after taking them out from the fridge/freezer.

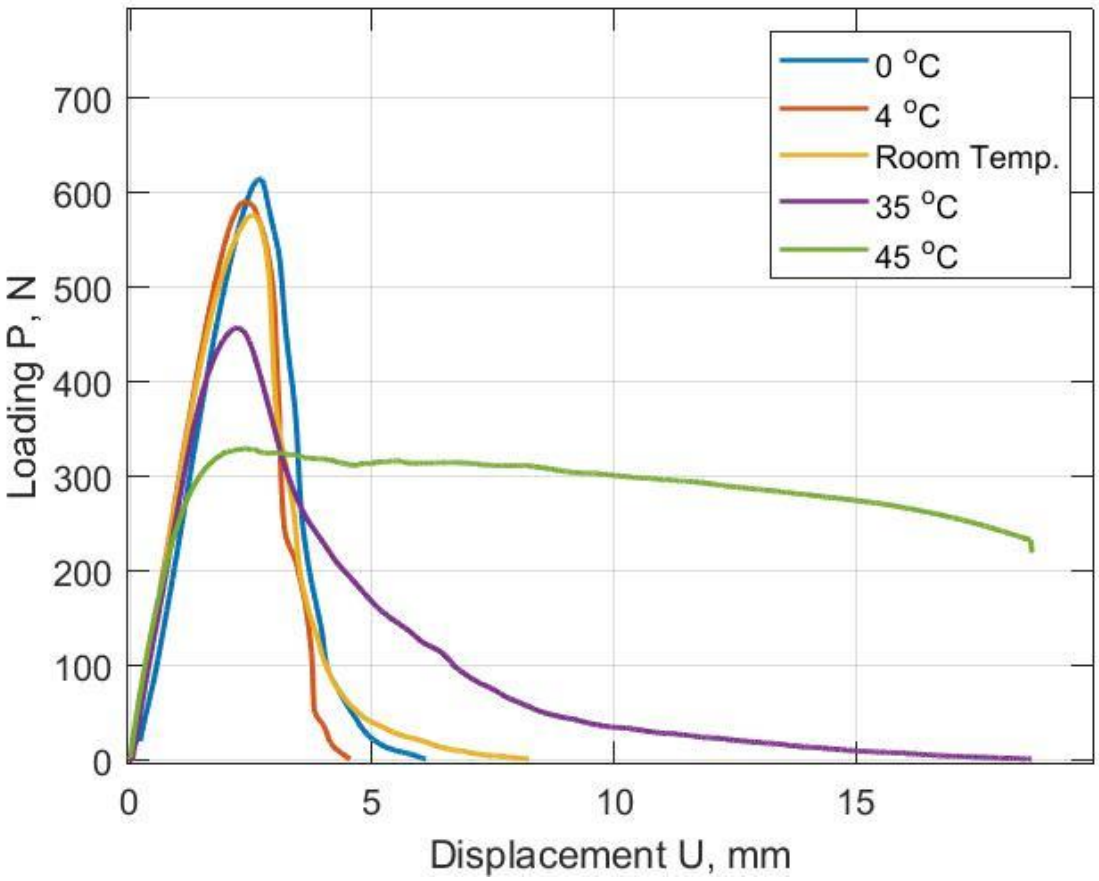

Figure 28: Load-displacement curve for 3D printed/rolled parts under different operating temperatures.

The experimental results explain how the material fracture behavior can be affected by the environmental working temperature. As we can see from the load-displacement curve (figure 28), the maximum load is higher for lower temperatures, while the total displacement before complete fracture is longer at higher temperatures. The part tested at 45℃ did not break, but the deformation reached the maximum allowed value due to the test's design limitations.

Also, we notice from the load-displacement curve (figure 28) and the part's fracture surfaces that the material acts as a brittle material at lower temperatures. On the other hand, at higher

temperatures, it acts as ductile material. At 55 ℃, there is no fracture but a material distortion; this means that at this temperature, the material exceeds the glass transition point, as shown in figure 29.

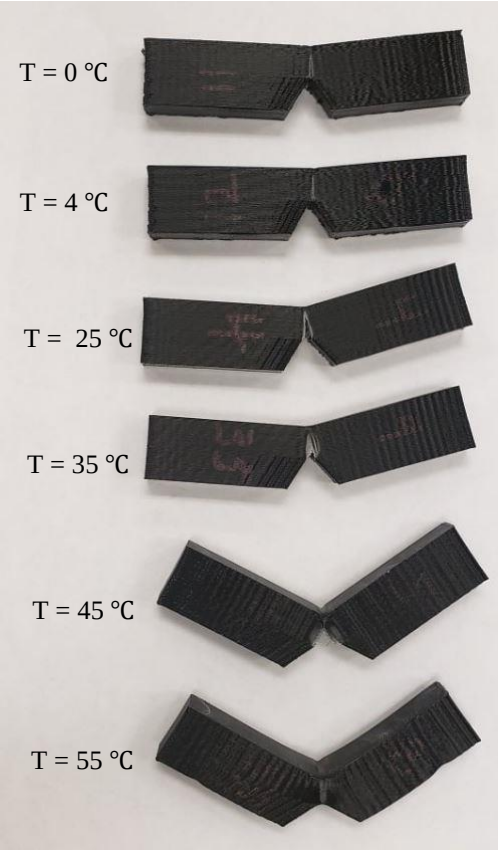

Figure 29: Schematic illustration for the fracture surface and crack propagation line for 3D printed/rolled parts under different operating temperatures.

The fracture behavior for the PLA plastic material at a range of temperatures comes as expected. Generally speaking, any thermoplastic material has a transition behavior from brittle to ductile as the operating temperature increases. Here we investigate the effect of this transition on the material fracture behavior. Figure 30 shows the maximum load versus the environmental temperature.

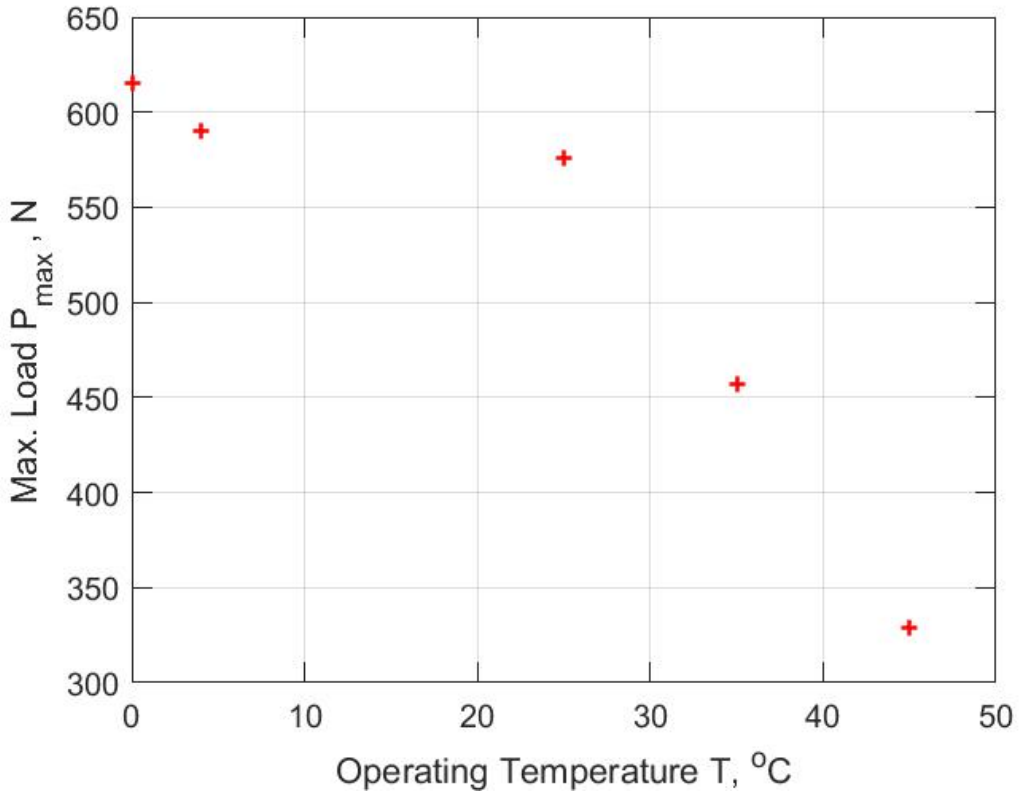

Figure 30: Maximum part's load, for fracture test, versus the environmental temperature.

5.5 Conclusion

In this chapter of our research, we investigate the fracture behavior of 3D-printed parts. We include in this study the effect of rolling after printing, the impact of printing at different layer heights, the impact of the filament-filament contact width versus the part thickness, and the impact of the operating temperature on 3D printed PLA thermoplastic material's fracture behavior.

We find, for the rolled 3d printed part, that the fracture properties get improved significantly. The maximum load is 92% higher, the crack initiation load is 99% higher, the critical stress intensity

factor is 164% higher, and the critical energy release rate is 277% higher than the baseline (no rolling) 3d printed samples. These results conclude the improvements in the fracture behavior due to rolling after printing.

We also investigate the effect of printing with lower layer height (0.24 mm versus 0.37 mm). we find a slight improvement in the fracture properties. 4%,13%, and 13% increase for maximum load, crack initiation load, and critical stress intensity factor, respectively. This concludes that the effect of rolling after printing on improving the material fracture properties is better than the effect of reducing the layer thickness, which means that the pressure that comes from the roller has a different impact from the pressure that comes from the printing nozzle (due to printing with lower layer hight).

We build a FE model to study the effect of the filament-filament contact width on the 3D printed part's fracture behavior. By comparing the effect of the contact width with the effect of the part thickness, we find that the stress intensity factor depends not only on filament-filament contact width but also on the contact angle between the two filaments.

We use the FE model results and curve fitting to find a relation between the stress intensity factor and the contact width. Then we used this relation to find the effect of rolling after printing techniques on the printed part's SIF. The stress intensity factor for the rolled part is 0.36% higher than the bulk material and 0.33% lower than the baseline part. This result concludes that rolling after printing improved the fracture behavior of the printed part to become closer to the behavior of the bulk material.

Finally, after we make sure that rolling after printing results in improving the fracture behavior of 3d printed part, we intended to study the effect of the operating temperature on the 3d printed/rolled part. As expected, lower temperature results in more brittle behavior, and higher temperature results in more ductile behavior. Maximum load at 45 equals around half of the maximum load at room temperature. While Maximum load at 0 equals around 1.06 of the maximum load at room temperature.

Chapter 6
Overall Conclusion

Our research has started since the first observation we made on our new technique of integrating ball rollers to apply in-situ pressure after depositing while the fused filament is still hot and soft. Our first observation reveals that the mechanical part strength and material toughness have improved in a significant amount. The improvement in the mechanical behavior is in both directions the longitudinal (along the filament depositing direction) and the transverse (90^o with the filament depositing direction).

The results of this study (Ravoori et al., 2021) spur us to model the effect of the rolling process. This model aims to find the impact of rolling-after-printing on the part's final height, the filament-filament contact width, the filament-filament adhesion, the part's mesostructure, and void fraction.

We conduct our model by using the JKR contact theory along with the theory of elasticity. We find the final part height and void fraction with good matching with the experimental results. We also recommend an isothermal contact between the filaments to improve the adhesion. To achieve isothermal contact, we suggest a pre-heating post-rolling configuration.

We perform a three-point bending test over a v-notch sample to further examine the rolled part's behavior. The outcomes of this project show a significant improvement in the rolled part's fracture properties in terms of fracture toughness and fracture energy. Then by employing a new fracture tool in ANSYS WORKBENCH (SMART crack propagation tool), we establish a mathematical

relation between the filament-filament contact width and the stress intensity factor. We implement this relation by using the results of our previous contact model to find the effect of rolling-after-printing on the crack propagating behavior.

Finally, we think that examining the behavior of printed/ rolled parts under different operating temperatures will provide essential knowledge of 3d printed PLA material behavior, which starts getting more attention in sundry industrial and medical applications.

Throughout this research, we prove that the rolling-after-printing technique is a promising process that can improve 3d printing by providing stronger and tougher parts and better controlling part's final geometries. We believe adopting this technology will take 3d printing to a higher level.

References

Abeykoon, C., Sri-Amphorn, P., & Fernando, A. (2020). Optimization of fused deposition modeling parameters for improved PLA and ABS 3D printed structures. *International Journal of Lightweight Materials and Manufacture*, *3*(3), 284–297. https://doi.org/10.1016/j.ijlmm.2020.03.003

Ahmed, A. A., & Susmel, L. (2017). Additively Manufactured PLA under static loading: Strength/cracking behaviour vs. deposition angle. *Procedia Structural Integrity*, *3*, 498–507. https://doi.org/10.1016/j.prostr.2017.04.060

Aliheidari, N., Christ, J., Ameli, A., Tripuraneni, R., & Nadimpalli, S. (2017). Optimizing fused deposition modeling 3D printing process for fracture resistance. *Annual Technical Conference - ANTEC, Conference Proceedings*, *2017-May*, 89–93.

Anderson, T. L. (2005). FRACTURE MECHANICS Fundamentals and Applications. In *Taylor & Francis Group* (Vol. 13, Issue 4). https://doi.org/10.1007/s42947-020-0181-2

Ayhan, A. O. (2011). Three-dimensional fracture analysis using tetrahedral enriched elements and fully unstructured mesh. *International Journal of Solids and Structures*, *48*(3–4), 492–505. https://doi.org/10.1016/j.ijsolstr.2010.10.012

Bechtel, S., Meisberger, M., Klein, S., Heib, T., Quirin, S., & Herrmann, H.-G. (n.d.). *materials Estimation of the Adhesion Interface Performance in Aluminum-PLA Joints by Thermographic Monitoring of the Material Extrusion Process*. https://doi.org/10.3390/ma13153371

Biresaw, G., & Carriere, C. J. (2001). Correlation between mechanical adhesion and interfacial properties of starch/biodegradable polyester blends. *Journal of Polymer Science, Part B: Polymer Physics*, *39*(9), 920–930. https://doi.org/10.1002/polb.1067

Brenken, B. (2017). *EXTRUSION DEPOSITION ADDITIVE MANUFACTURING OF FIBER REINFORCED SEMI-CRYSTALLINE POLYMERS by School of Aeronautics & Astronautics*. *December*, 248.

Casavola, C., Cazzato, A., Moramarco, V., & Pappalettere, C. (2016). Orthotropic mechanical properties of fused deposition modelling parts described by classical laminate theory. *Materials and Design*, *90*, 453–458. https://doi.org/10.1016/j.matdes.2015.11.009

Chaudhury, M. K., Weaver, T., Hui, C. Y., Kramer, E. J., Chaudhury, M. K., & Weaver, T. (1996). *Adhesive contact of cylindrical lens and a flat sheet*. *30*. https://doi.org/10.1063/1.362819

Ciavarella, M., Joe, J., Papangelo, A., & Barber, J. R. (2019). The role of adhesion in contact mechanics. *Journal of the Royal Society Interface*, *16*(151). https://doi.org/10.1098/rsif.2018.0738

COEFFICIENT OF THERMAL EXPANSION FOR VARIOUS MATERIALS AT DIFFERENT

TEMPERATURES. (2004). www.balseal.com.

Comninou, M., Dundurs, J., & Barber, J. R. (1981). Planar hertz contact with heat conduction. *Journal of Applied Mechanics, Transactions ASME*, *48*(3), 549–554. https://doi.org/10.1115/1.3157672

Comninou, Maria, Barber, J. R., & Dundurs, J. (1981). Heat conduction through a flat punch. *Journal of Applied Mechanics, Transactions ASME*, *48*(4), 871–875. https://doi.org/10.1115/1.3157748

Coogan, T. J., & Kazmer, D. O. (2017). Bond and part strength in fused deposition modeling. *Rapid Prototyping Journal*, *23*(2), 414–422. https://doi.org/10.1108/RPJ-03-2016-0050

Corapi, D., Morettini, G., Pascoletti, G., & Zitelli, C. (2019). Characterization of a polylactic acid (PLA) produced by Fused Deposition Modeling (FDM) technology. *Procedia Structural Integrity*, *24*(2019), 289–295. https://doi.org/10.1016/j.prostr.2020.02.026

Costa, S. F., Duarte, F. M., & Covas, J. A. (2017). Estimation of filament temperature and adhesion development in fused deposition techniques. *Journal of Materials Processing Technology*, *245*, 167–179. https://doi.org/10.1016/j.jmatprotec.2017.02.026

Cuan-Urquizo, E., Yang, S., & Bhaskar, A. (2015). Mechanical characterisation of additively manufactured material having lattice microstructure. *IOP Conference Series: Materials Science and Engineering*, *74*(1), 012004. https://doi.org/10.1088/1757-899X/74/1/012004

Cuan-Urquizo, Enrique, Barocio, E., Tejada-Ortigoza, V., Pipes, R. B., Rodriguez, C. A., & Roman-Flores, A. (2019). Characterization of the mechanical properties of FFF structures and materials: A review on the experimental, computational and theoretical approaches. *Materials*, *16*(6). https://doi.org/10.3390/ma12060895

Diegel, O., Nordin, A., & Motte, D. (2019). *Additive Manufacturing Technologies*. https://doi.org/10.1007/978-981-13-8281-9_2

Dunn, R. M., Hart, K. R., & Wetzel, E. D. (2019). Improving fracture strength of fused filament fabrication parts via thermal annealing in a printed support shell. *Progress in Additive Manufacturing*, *4*(3), 233–243. https://doi.org/10.1007/s40964-019-00081-x

Farah, S., Anderson, D. G., & Langer, R. (2016). Physical and mechanical properties of PLA, and their functions in widespread applications — A comprehensive review. *Advanced Drug Delivery Reviews*, *107*, 367–392. https://doi.org/10.1016/j.addr.2016.06.012

Fonseca, J., Ferreira, I. A., de Moura, M. F. S. F., Machado, M., & Alves, J. L. (2019). Study of the interlaminar fracture under mode I loading on FFF printed parts. *Composite Structures*, *214*(November 2018), 316–324. https://doi.org/10.1016/j.compstruct.2019.02.005

Gámez-Pérez, J., Velazquez-Infante, J. C., Franco-Urquiza, E., Pages, P., Carrasco, F., Santana, O. O., & Maspoch, M. L. (2011). Fracture behavior of quenched poly(lactic acid). *Express Polymer Letters*, *5*(1), 82–91. https://doi.org/10.3144/expresspolymlett.2011.9

Gardan, J., Makke, A., & Recho, N. (2018). Improving the fracture toughness of 3D printed thermoplastic polymers by fused deposition modeling. *International Journal of Fracture*, *210*(1–2), 1–15. https://doi.org/10.1007/s10704-017-0257-4

Hart, K. R., & Wetzel, E. D. (2017). Fracture behavior of additively manufactured acrylonitrile butadiene styrene (ABS) materials. *Engineering Fracture Mechanics*, *177*, 1–13. https://doi.org/10.1016/j.engfracmech.2017.03.028

Herrera Franco, P. J., & Valadez-González, A. (2005). Fiber-matrix adhesion in natural fiber composites. In *Natural Fibers, Biopolymers, and Biocomposites*. https://doi.org/10.1201/9780203508206.ch6

Huang, B., & Singamneni, S. (2015). Raster angle mechanics in fused deposition modelling. *Journal of Composite Materials*, *49*(3), 363–383. https://doi.org/10.1177/0021998313519153

Jamshidian, M., Tehrany, E. A., Imran, M., Jacquot, M., & Desobry, S. (2010). Poly-Lactic Acid: Production, Applications, Nanocomposites, and Release Studies. *Comprehensive Reviews in Food Science and Food Safety*, *9*(5), 552–571. https://doi.org/10.1111/j.1541-4337.2010.00126.x

Johnson, K. L., Kendall, K., & Roberts, A. D. (1971). Surface energy and the contact of elastic solids. *Proceedings of the Royal Society of London. A. Mathematical and Physical Sciences*, *324*(1558), 301–313. https://doi.org/10.1098/rspa.1971.0141

K. L. Johnson - Contact mechanics-Cambridge University Press (1985).

Kisin, S., Vukić, J. B., Van Der Varst, P. G. T., De With, G., & Koning, C. E. (2007). Estimating the polymer - Metal work of adhesion from molecular dynamics simulations. *Chemistry of Materials*, *19*(4), 903–907. https://doi.org/10.1021/cm0621702

Kulkarni, P., & Dutta, D. (1999). Deposition strategies and resulting part stiffnesses in fused deposition modeling. *Journal of Manufacturing Science and Engineering, Transactions of the ASME*, *121*(1), 93–103. https://doi.org/10.1115/1.2830582

Leguillon, D., Quesada, D., Putot, C., & Martin, E. (2007). Prediction of crack initiation at blunt notches and cavities - size effects. *Engineering Fracture Mechanics*, *74*(15), 2420–2436. https://doi.org/10.1016/j.engfracmech.2006.11.008

Lim, L. T., Auras, R., & Rubino, M. (2008). Processing technologies for poly(lactic acid). *Progress in Polymer Science (Oxford)*, *33*(8), 820–852. https://doi.org/10.1016/j.progpolymsci.2008.05.004

McIlroy, C., & Olmsted, P. D. (2017). Deformation of an amorphous polymer during the fused-filament-fabrication method for additive manufacturing. *Journal of Rheology*, *61*(2), 379–397. https://doi.org/10.1122/1.4976839

Ngo, T. D., Kashani, A., Imbalzano, G., Nguyen, K. T. Q., & Hui, D. (2018). Additive manufacturing (3D printing): A review of materials, methods, applications and challenges. *Composites Part B: Engineering*, *143*, 172–196. https://doi.org/10.1016/j.compositesb.2018.02.012

Noori, H. (2019). Interlayer fracture energy of 3D-printed PLA material. *International Journal of Advanced Manufacturing Technology*, *101*(5–8), 1959–1965. https://doi.org/10.1007/s00170-018-3031-5

Patanwala, H. S., Hong, D., Vora, S. R., Bognet, B., & Ma, A. W. K. (n.d.). *The Microstructure and Mechanical Properties of 3D Printed Carbon Nanotube-Polylactic Acid Composites*. https://doi.org/10.1002/pc.24494

Peng, X., & Huang, G. (2016). International Journal of Solids and Structures Adhesive contact between dissimilar cylinders subject to a temperature difference. *International Journal of Solids and Structures*, *90*, 22–29. https://doi.org/10.1016/j.ijsolstr.2016.04.014

Pérez, C. J., Eisenberg, P., Bernal, C., & Pérez, E. (2018). Mechanical evaluation of polylactic acid (PLA) based composites reinforced with different calcium phosphates. *Materials Research Express*, *5*(10). https://doi.org/10.1088/2053-1591/aadb5b

Popescu, D., Zapciu, A., Amza, C., Baciu, F., & Marinescu, R. (2018). FDM process parameters influence over the mechanical properties of polymer specimens: A review. *Polymer Testing*, *69*(May), 157–166. https://doi.org/10.1016/j.polymertesting.2018.05.020

Prajapati, H., Ravoori, D., Woods, R. L., & Jain, A. (2018). Measurement of anisotropic thermal conductivity and inter-layer thermal contact resistance in polymer fused deposition modeling (FDM). *Additive Manufacturing*, *21*(February), 84–90. https://doi.org/10.1016/j.addma.2018.02.019

Prajapati, H., Salvi, S. S., Ravoori, D., Qasaimeh, M., Adnan, A., & Jain, A. (2021). Improved print quality in fused filament fabrication through localized dispensing of hot air around the deposited filament. *Additive Manufacturing*, *40*(February), 101917. https://doi.org/10.1016/j.addma.2021.101917

Rane, R., Kulkarni, A., Prajapati, H., Taylor, R., Jain, A., & Chen, V. (2020). Post-process effects of isothermal annealing and initially applied static uniaxial loading on the ultimate tensile strength of fused filament fabrication parts. *Materials*, *13*(2). https://doi.org/10.3390/ma13020352

Ravi, A. K., Deshpande, A., & Hsu, K. H. (2016). An in-process laser localized pre-deposition heating approach to inter-layer bond strengthening in extrusion based polymer additive manufacturing. *Journal of Manufacturing Processes*, *24*, 179–185. https://doi.org/10.1016/j.jmapro.2016.08.007

Ravoori, D., Prajapati, H., Talluru, V., Adnan, A., & Jain, A. (2019a). Nozzle-integrated pre-deposition and post-deposition heating of previously deposited layers in polymer extrusion based additive manufacturing. *Additive Manufacturing*, *28*(June), 719–726. https://doi.org/10.1016/j.addma.2019.06.006

Ravoori, D., Prajapati, H., Talluru, V., Adnan, A., & Jain, A. (2019b). Nozzle-integrated pre-deposition and post-deposition heating of previously deposited layers in polymer extrusion based additive manufacturing. *Additive Manufacturing*, *28*(May), 719–726. https://doi.org/10.1016/j.addma.2019.06.006

Ravoori, D., Salvi, S., Prajapati, H., Qasaimeh, M., Adnan, A., & Jain, A. (2021). Void reduction in fused filament fabrication (FFF) through in situ nozzle-integrated compression rolling of deposited filaments. *Virtual and Physical Prototyping*, *0*(2), 1–14. https://doi.org/10.1080/17452759.2021.1890986

Rezaee, A., & Adnan, A. (2018a). On the elastic stress singularities and mode I notch stress intensity factor for 3D printed polymers. *Engineering Fracture Mechanics*, *204*(May), 235–245. https://doi.org/10.1016/j.engfracmech.2018.09.035

Rezaee, A., & Adnan, A. (2018b). On the elastic stress singularities and mode I notch stress intensity factor for 3D printed polymers. *Engineering Fracture Mechanics*, *204*(May), 235–245. https://doi.org/10.1016/j.engfracmech.2018.09.035

Schaul, J. S. (1985). Polymer processing. In *Chemical and Engineering News* (Vol. 63, Issue 37).

Seppala, J. E., Hoon Han, S., Hillgartner, K. E., Davis, C. S., & Migler, K. B. (2017). Weld formation during material extrusion additive manufacturing. *Soft Matter*, *13*(38), 6761–6769. https://doi.org/10.1039/c7sm00950j

Serdeczny, M. P., Comminal, R., Pedersen, D. B., & Spangenberg, J. (2020). Experimental and analytical study of the polymer melt flow through the hot-end in material extrusion additive manufacturing. *Additive Manufacturing*, *32*(October 2019), 100997. https://doi.org/10.1016/j.addma.2019.100997

Siddall, J. N. (2019). Welding, Brazing, and Soldering. *Mechanical Design*, 155–155. https://doi.org/10.3138/9781487579890-121

Solarski, S., Ferreira, M., & Devaux, E. (2007). Thermal and mechanical characteristics of polylactide filaments drawn at different temperatures. *Journal of the Textile Institute*, *98*(3), 227–236. https://doi.org/10.1080/00405000701476179

Standard, a. (1996). Standard Test Methods for Plane-Strain Fracture Toughness and Strain Energy Release Rate of Plastic Materials. *Annul Book of ASTM Standards*, *99*(Reapproved), 1–9. https://doi.org/10.1520/D5045-99R07E01.2

Subramaniam, S. R., Samykano, M., Selvamani, S. K., Ngui, W. K., Kadirgama, K., Sudhakar, K., & Idris, M. S. (2019). Preliminary investigations of polylactic acid (PLA) properties. *AIP Conference Proceedings*, *2059*(January). https://doi.org/10.1063/1.5085981

Suérez, J. C., Miguel, S., Pinilla, P., & López, F. (2008). Molecular dynamics simulation of polymer-metal bonds. *Journal of Adhesion Science and Technology*, *22*(13), 1387–1400. https://doi.org/10.1163/156856108X305732

Todo, M. (2007). Effect of unidirectional drawing process on fracture behavior of poly(l-lactide). *Journal of Materials Science*, *42*(4), 1393–1396. https://doi.org/10.1007/s10853-006-1312-0

Valerga, A. P., Batista, M., Salguero, J., & Girot, F. (2018). Influence of PLA filament conditions on characteristics of FDM parts. *Materials*, *11*(8). https://doi.org/10.3390/ma11081322

Williams, J. A., & Dwyer-Joyce, R. S. (2000). Contact between solid surfaces. *Modern Tribology Handbook: Volume One: Principles of Tribology*, 121–162. https://doi.org/10.1007/978-1-4684-0335-0_3

Yang, F., & Pitchumani, R. (2002). Healing of thermoplastic polymers at an interface under nonisothermal conditions. *Macromolecules*, *35*(8), 3213–3224.

https://doi.org/10.1021/ma010858o

Yousefzade, O., Jeddi, J., Vazirinasab, E., & Garmabi, H. (2019). Poly(lactic acid) phase transitions in the presence of nano calcium carbonate: Opposing effect of nanofiller on static and dynamic measurements. *Journal of Thermoplastic Composite Materials*, *32*(3), 312–327. https://doi.org/10.1177/0892705718759386

Zhao, Y., Chen, Y., & Zhou, Y. (2019). Novel mechanical models of tensile strength and elastic property of FDM AM PLA materials: Experimental and theoretical analyses. *Materials and Design*, *181*, 108089. https://doi.org/10.1016/j.matdes.2019.108089

Zhou, C., Guo, H., Li, J., Huang, S., & Li, H. (2016). *RSC Advances mechanical properties*. 113762–113772. https://doi.org/10.1039/c6ra23610c

Zhou, M., Fu, L., Jiang, F., Jiang, B., & Drummer, D. (2020). Atomistic investigation on the wetting behavior and interfacial joining of polymer-metal interface. *Polymers*, *12*(8). https://doi.org/10.3390/POLYM12081696

Ziemian, C. W., Ziemian, R. D., & Haile, K. V. (2016). Characterization of stiffness degradation caused by fatigue damage of additive manufactured parts. *Materials and Design*, *109*, 209–218. https://doi.org/10.1016/j.matdes.2016.07.080

List of Figures:

List of Tables:

Appendixes:

Appendix A: Mathematical Formulation

JKR contact theory states that:

$$G = \Delta\gamma \tag{1}$$

Where G is the strain release rate, and $\Delta\gamma$ is the thermodynamic work of adhesion with a unit of J/m^2. Substituting the value of strain energy release rate G as a function of mode one and mode two stress intensity factor, K_I and K_{II} respectively, (Johnson et al., 1971), we can get

$$\frac{K_I^2+K_{II}^2}{2E^*} = \Delta\gamma \tag{2}$$

Where $E^*$is the effective stiffness and equals to:

$$\frac{1}{E^*} = \frac{1-{\nu_1}^2}{E_1} + \frac{1-{\nu_2}^2}{E_2} \tag{3}$$

Where E_i and ν_i are the modulus of elasticity and Poisson's ratio for i cylinder, respectively. and But we know that K_I and K_{II} can be expressed as a function of the normal stress $p(x)$ and the shear stress $\tau(x)$ along the contact width 2a as follows (Anderson, 2005):

$$K_I = -\lim_{x\to a}\sqrt{2\pi(a-x)}p(x) \tag{4}$$

$$K_{II} = \lim_{x \to a} \sqrt{2\pi(a - x)}\tau(x) \tag{5}$$

So, to find the contact width 2a, first, we need to find the normal and shear stress distributions $p(x)$ and $\tau(x)$ along the contact width, assuming that the work of adhesion $\Delta\gamma$ between the two materials is known. We apply the theory of elasticity on the two cylinders made of two different materials having two different temperatures in contact to solve for $p(x)$ and $\tau(x)$. In this formulation, the contact surface normal stresses $p(x)$ arises from the normal applied load and the shear stress $\tau(x)$ is generated from the difference in the temperatures and the thermal properties of the two materials. When heat is transferred from the hot material to the cold material, in principle, the hot one will gradually shrink, but the cold one will expand, resulting in shear stress between the two surfaces.

The contact conditions between the cylinders assuming that no slip occurs can be expressed as follows (K. L. Johnson, 1985):

$$\frac{\partial u_{y_1}}{\partial x} - \frac{\partial u_{y_2}}{\partial x} = -\frac{x}{R^*} \tag{6}$$

$$\frac{\partial u_{x_1}}{\partial x} - \frac{\partial u_{x_2}}{\partial x} = 0 \tag{7}$$

Where: $\frac{1}{R^*} = \frac{1}{R_1} + \frac{1}{R_2}$, u_x is the deformation along the x-direction and u_y is the deformation along y-direction. The governing equations of the general case, first we have the equilibrium equation:

$$\begin{Bmatrix} \frac{\partial \sigma_{xy}}{\partial y} + \frac{\partial \sigma_{xx}}{\partial x} = 0 \\ \frac{\partial \sigma_{xy}}{\partial x} + \frac{\partial \sigma_{yy}}{\partial y} = 0 \end{Bmatrix} \tag{8}$$

Then we have the steady-state condition that leads to the heat equation between the two cylinders:

$$\{\nabla^2\theta = 0\} \tag{9}$$

Let us consider the strain compatibility equation:

$$\frac{\partial^2\varepsilon_{xx}}{\partial y^2} + \frac{\partial^2\varepsilon_{yy}}{\partial x^2} - 2\frac{\partial^2\varepsilon_{xy}}{\partial x\,\partial y} = 0 \tag{10}$$

Assuming plane stain problem, the thermal stress-strain constitutive equations for an isotropic linear elastic material takes the following forms:

$$\varepsilon_{xx} = \frac{1-\nu}{E}\left[(1-\nu)\sigma_{xx} - \nu\sigma_{yy}\right] + \alpha(1+\nu)\theta \tag{11}$$

$$\varepsilon_{yy} = \frac{1-\nu}{E}\left[(1-\nu)\sigma_{yy} - \nu\sigma_{xx}\right] + \alpha(1+\nu)\theta \tag{12}$$

$$\varepsilon_{xy} = \frac{1+\nu}{E}\sigma_{xy} \tag{13}$$

Where:

$$\varepsilon_{xx} = \frac{\partial u_x}{\partial x},\ \varepsilon_{yy} = \frac{\partial u_y}{\partial y} \text{ and } \varepsilon_{xy} = \varepsilon_{yx} = \frac{1}{2}\left(\frac{\partial u_x}{\partial y} + \frac{\partial u_y}{\partial x}\right) \tag{14}$$

Substituting the constitutive equations 11, 12, and 13 into the compatibility equation will result in:

$$\frac{\partial^2\sigma_{xx}}{\partial y^2} + \frac{\partial^2\sigma_{yy}}{\partial x^2} - \nu\nabla^2\left(\sigma_{xx}+\sigma_{yy}\right) - 2\frac{\partial^2\sigma_{xy}}{\partial x\,\partial y} + \alpha E\nabla^2\theta = 0 \tag{15}$$

The thermal and mechanical boundary conditions along the contact width can be stated as in equations 16, 17, 18, and 19, where outside the contact width there are no stresses applied and no heat transferred (K. L. Johnson, 1985) (Maria Comninou et al., 1981) (M. Comninou et al., 1981).

$$\begin{Bmatrix} \sigma_{yy_i}(x,0) = -p(x) \\ \sigma_{xy_i}(x,0) = \tau(x) \end{Bmatrix}, \ |x| \le a \tag{16}$$

$$\begin{Bmatrix} \sigma_{xy_i}(x,0) = 0 \\ \sigma_{yy_i}(x,0) = 0 \end{Bmatrix}, \ |x| \ge a \tag{17}$$

$$\begin{Bmatrix} T_i(x,0) = T_s(x) \\ -k_i \frac{\partial \theta_i(x,0)}{\partial y} = q(x) \end{Bmatrix}, \quad |x| \le a \tag{18}$$

$$\left\{ -k_i \frac{\partial \theta_i(x,0)}{\partial y} = 0 \right\}, |x| \ge a \tag{19}$$

Where T_i is the temperature distribution, T_s is the contact surface temperature, k is the thermal conductivity, $q(x)$ is the heat flux from the hot to the cold cylinder, a is the contact half-width, and $\theta = T - T_o$ where T_o is the initial temperature before contact.

Furthermore, the following force balance equations along the contact width should be fulfilled where we have a no-slip condition:

$$\int_{-a}^{a} p(x)dx = P \tag{20}$$

$$\int_{-a}^{a} \tau(x) = 0 \tag{21}$$

The solution to this formulation involves solving the boundary value problem (Peng & Huang, 2016) using the Airy stress function and Fourier integral transform method, and then obtaining the general solution to the normal and shear stresses distribution can be found in (K. L. Johnson, 1985).

$$p(x) = \frac{E^*}{2R^*}(a^2 - x^2)^{1/2} + \left(\frac{P}{\pi} - \frac{E^* a^2}{4R^*}\right)(a^2 - x^2)^{-1/2} - (a^2 - x^2)^{-\frac{1}{2}} \frac{E^* \varepsilon_1}{2\pi C} \int_{-a}^{a} \frac{(a^2 - t^2)^{\frac{1}{2}}}{x - t} \arcsin\left(\frac{t}{a}\right) dt \quad (22)$$

$$\tau(x) = \frac{E^* \varepsilon_2}{2} \frac{x}{(a^2 - x^2)^{1/2}} \quad (23)$$

Where

$$\frac{1}{R^*} = \frac{1}{R_1} + \frac{1}{R_2} \quad (24)$$

$$\frac{1}{E^*} = \frac{(1 - {\nu_1}^2)}{E_1} + \frac{(1 - {\nu_2}^2)}{E_2} \quad (25)$$

By inserting equations 22 and 23 into equations 4 and 5:

$$K_I = \frac{\sqrt{\pi} E^*}{4R^*} a^{3/2} - \frac{P}{\sqrt{\pi a}} + \frac{E^* \varepsilon_1}{C} \sqrt{\frac{a}{\pi}} \quad (26)$$

$$K_{II} = \frac{E^* \varepsilon_2}{2} \sqrt{\pi a} \quad (27)$$

By considering the JKR model and substituting back the new formulas for K_I and K_{II} in equation 2, and by solving for P, we can get P the applied force as a function of 'a' the contact half-width as in equation 28

$$P = \frac{\pi E^*}{4R^*}a^2 + \frac{E^*\varepsilon_1}{C}a + \sqrt{(2\pi\Delta\gamma E^*)a - \frac{(\pi E^*\varepsilon_2)^2}{4}a^2} \tag{28}$$

In the past, (Chaudhury et al., 1996) studied the adhesive contact for spherical and cylindrical surfaces on a flat sheet. The study was focused on isothermal contact between the surfaces. To express the pressure in a nondimensional form, we relate it to the results of the nonisothermal contact where the pressure and the half contact width can be calculated as:

$$P_{IC} = \frac{3}{4}\sqrt[3]{4\pi E^* R^* \Delta\gamma^2} \tag{29}$$

$$a_{IC} = \sqrt[3]{\frac{2\Delta\gamma R^{*2}}{\pi E^*}} \tag{30}$$

Then, the normalized stress $\widehat{P} = \frac{P}{P_{IC}}$ and contact half-width $\hat{a} = \frac{a}{a_{IC}}$ can be correlated in the following equation:

$$\widehat{P} = \frac{1}{3}\hat{a}^2 + \frac{4}{3}(2\pi^2)^{-1/3}\left(\frac{E^*R^*}{\Delta\gamma}\right)^{1/3}\frac{\varepsilon_1}{\ln(10)}\hat{a} - \sqrt{\frac{16}{9}\hat{a} - \frac{4}{9}\left(\frac{\pi}{2}\right)^{2/3}\left(\left(\frac{E^*R^*}{\Delta\gamma}\right)^{1/3}\varepsilon_2\hat{a}\right)^2} \tag{31}$$

Where the corresponding thermal strains ε_1 and ε_2 are equal to:

$$\varepsilon_1 = \mathrm{k}^*\left(T_{o_2} - T_{o_1}\right)(\delta_1 - \delta_2) \tag{32}$$

$$\varepsilon_2 = \mathrm{k}^*\left(T_{o_2} - T_{o_1}\right)(\delta_1 + \delta_2) \tag{33}$$

Where :

$$\delta_1 = \alpha_1 \frac{(1+\nu_1)}{k_1} \tag{34}$$

$$\delta_2 = \alpha_2 \frac{(1+\nu_2)}{k_2} \tag{35}$$

$$\frac{1}{\mathrm{k}^*} = \frac{1}{k_1} + \frac{1}{k_2} \tag{36}$$

Appendix B: Material Properties

For the sake of our study, k = $0.196\,\frac{\mathrm{w}}{\mathrm{m.k}}$ at 130℃ and k =$0.170\,\frac{\mathrm{w}}{\mathrm{m.k}}$ at 90℃. In the previous work (Ravoori et al., 2021), the 440C stainless steel roller ball was used. At 110℃, Young's modulus, E, and thermal conductivity, k, of stainless steel are 200 GPa and 24.2 $\frac{\mathrm{w}}{\mathrm{m.k}}$ (Siddall, 2019), respectively. The coefficient of thermal expansion, CTE, for 440C stainless steel is equal to $10.1 \times 10^{-6}\ \frac{1}{℃}$ (BALSEAL, 2004) and the CTE for PLA is equal to $70\times 10^{-6}\ \frac{1}{℃}$ (Lim et al., 2008). For semicrystalline PLA, the density at 140 oC has been found to be equal to 1.152 (g/cm3). The density increases to 1.36 (g/cm3) at room temperature.(Herrera Franco & Valadez-González, 2005).

Table 3: Thermal and mechanical properties of the used material at working temperatures.

	Temperature T_i (°C)	Modulus of elasticity E_i (MPa)	Thermal conductivity k_i ($\frac{\mathrm{w}}{\mathrm{m.k}}$)	Poison's ratio ν_i	Thermodynamics work of adhesion. $\Delta\gamma$ ($\frac{\mathrm{J}}{\mathrm{m}^2}$)	Coefficient of thermal expansion α_i ($\frac{1}{℃}$)
PLA	130	75.6	0.196	0.3	0.083	70×10^{-6}
	90	24.1	0.170			
Steel	110	200×10^{3}	24.2	0.3	1.93	10.1×10^{-6}

Appendix C: Plots of Pressure vs. Contact Half-width for The Four Contact Cases

Case # 1:

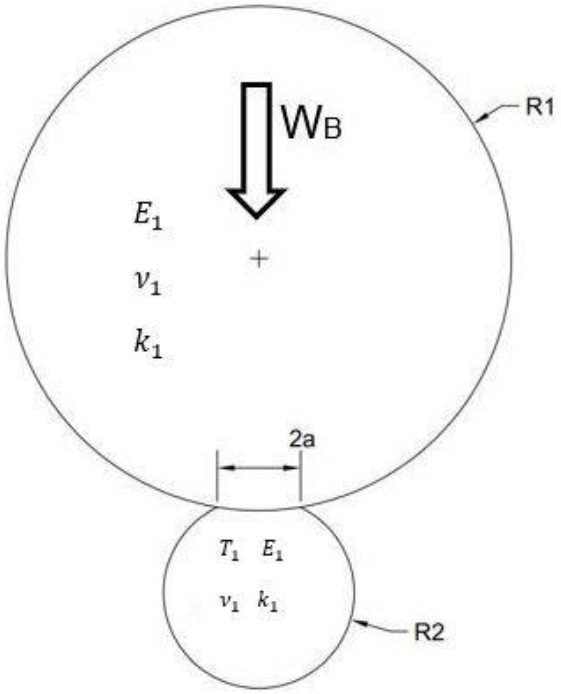

Figure 31: Schematic diagram to illustrate the case of steel ball in contact with PLA filament.

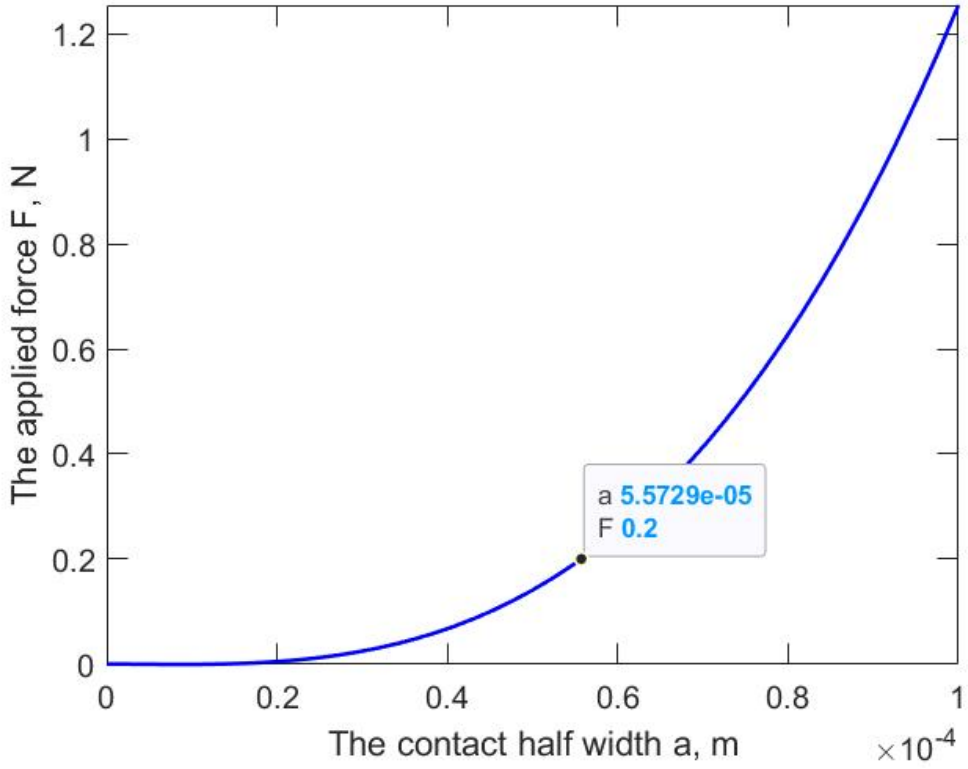

Figure 32: Plot of the applied load as a function of the contact half-width for the steel ball-PLA filament contact case.

Case # 2 :

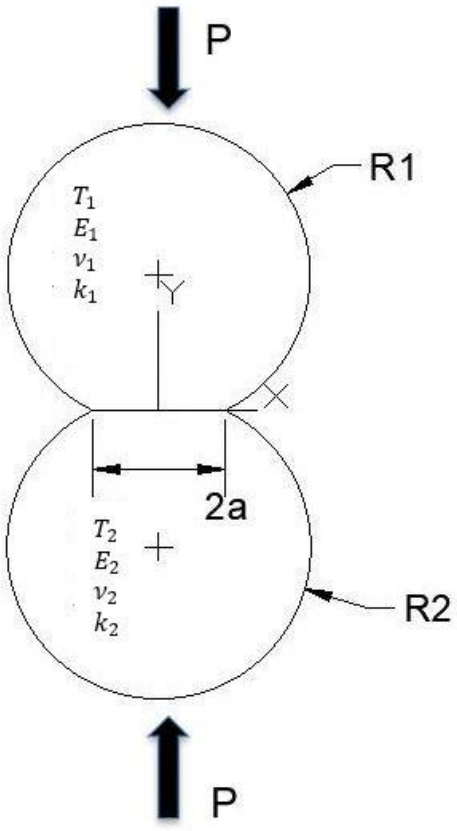

Figure 33: Schematic to illustrate the case of two cylindrical filaments in contact under an applied pressure of ball weight.

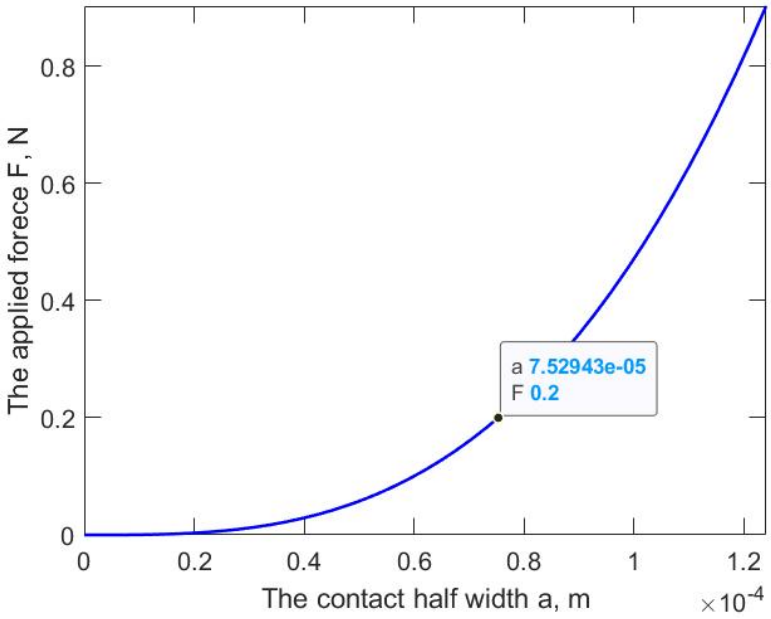

Figure 34: Plot of the applied load as a function of the contact half-width for PLA-PLA filament contact between the first and the second filament.

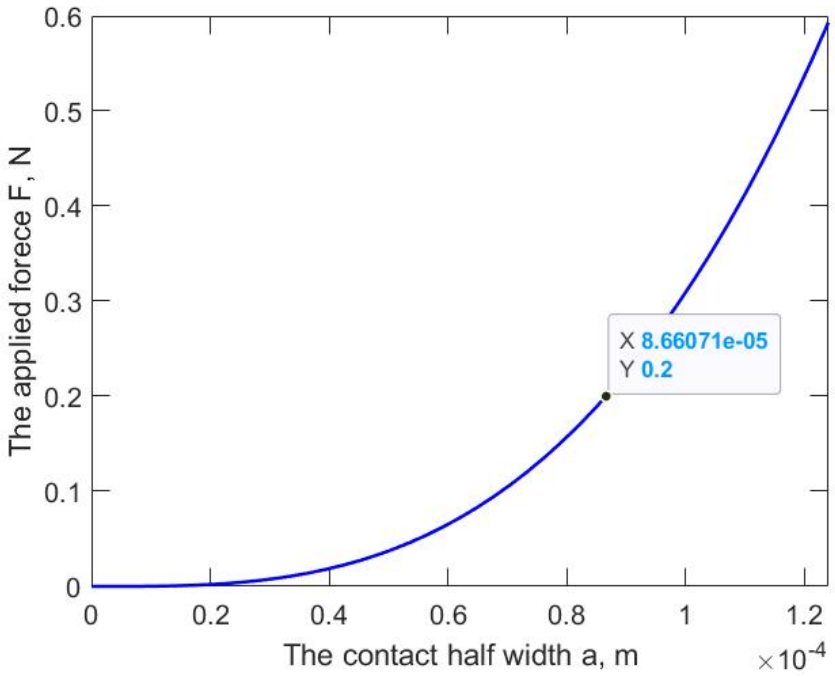

Figure 35: Plot of the applied load as a function of the contact half-width for PLA-PLA filament contact between 0.4 mm diameter filaments.

Case # 3:

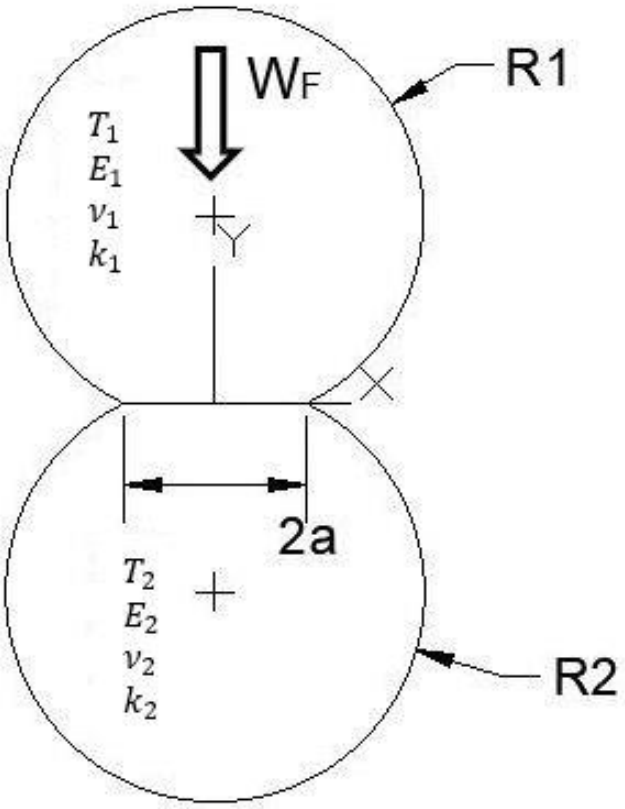

Figure 36: Schematic to illustrate the case of two cylindrical filaments in contact under an applied pressure of upper filament weight.

Case # 3 - Part # 1: With no swell effect

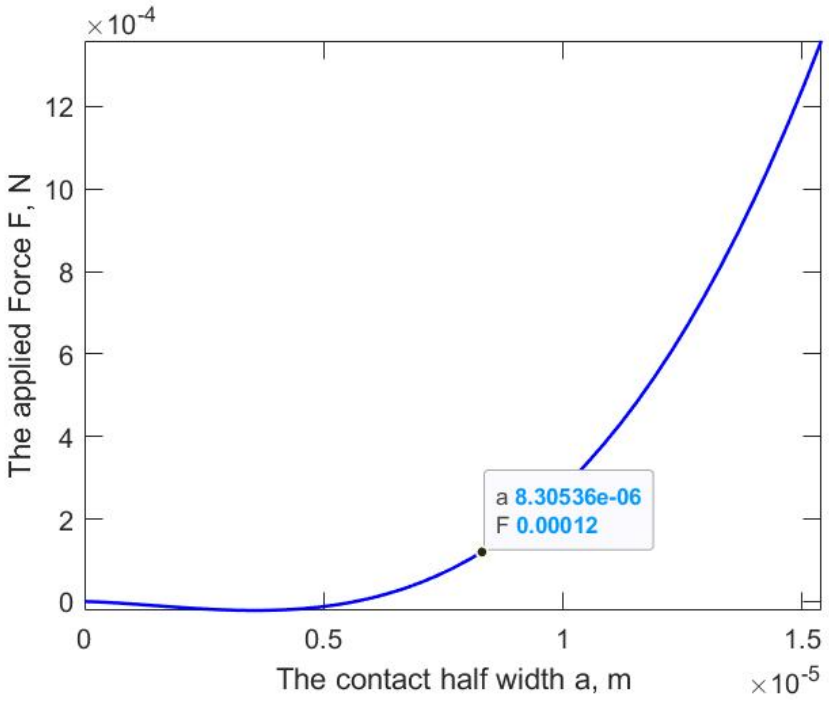

Figure 37: Plot of the applied load as a function of the contact half-width for PLA-PLA filament contact between 0.2 mm and 0.4 mm diameter filaments.

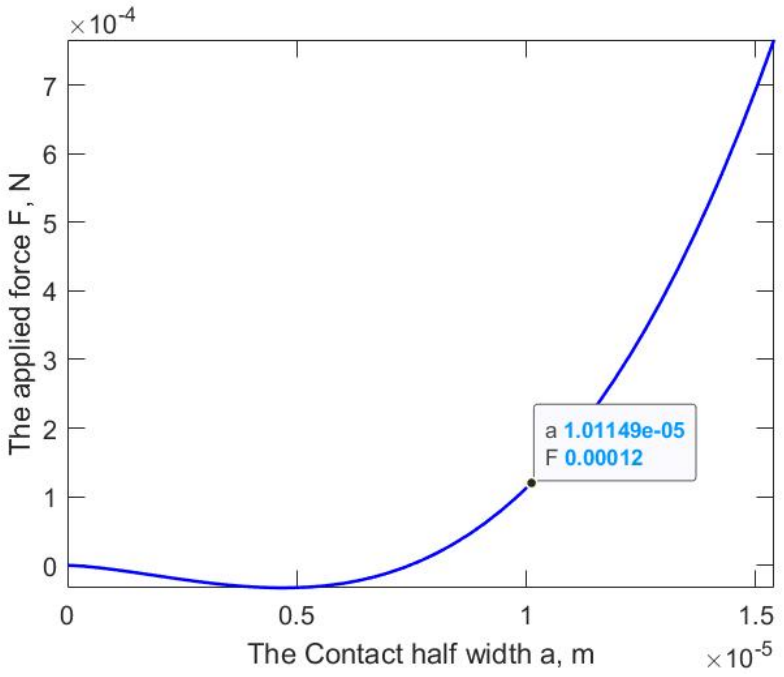

Figure 38: Plot of the applied load as a function of the contact half-width for PLA-PLA filament contact between 0.4 mm diameter filaments.

Case # 3 - Part # 2: With swell effect

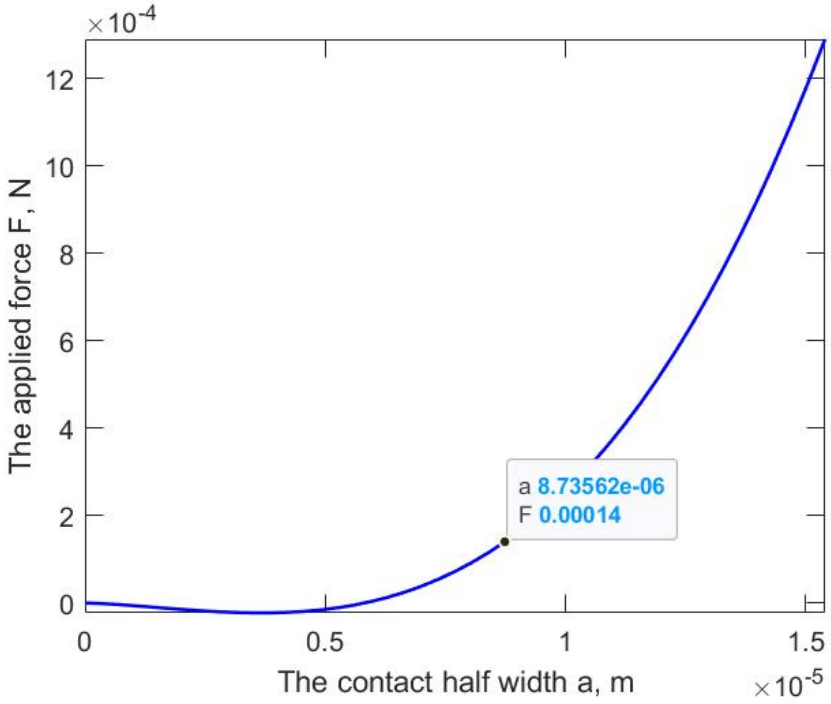

Figure 39: Plot of the applied load as a function of the contact half-width for PLA-PLA filament contact between 0.2 mm and 0.44 mm diameter filaments.

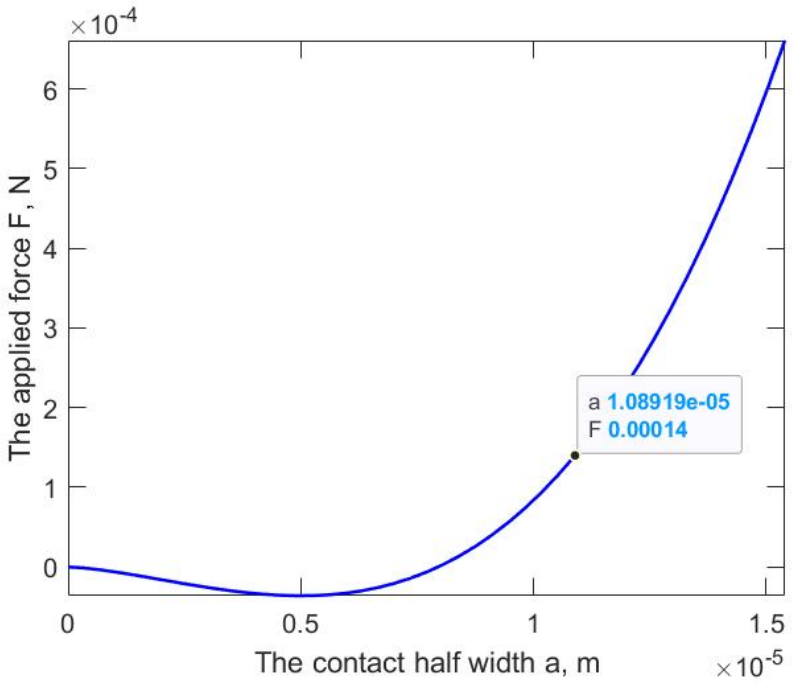

Figure 40: Plot of the applied load as a function of the contact half-width for PLA-PLA filament contact between 0.44 mm diameter filaments.

Case # 4:

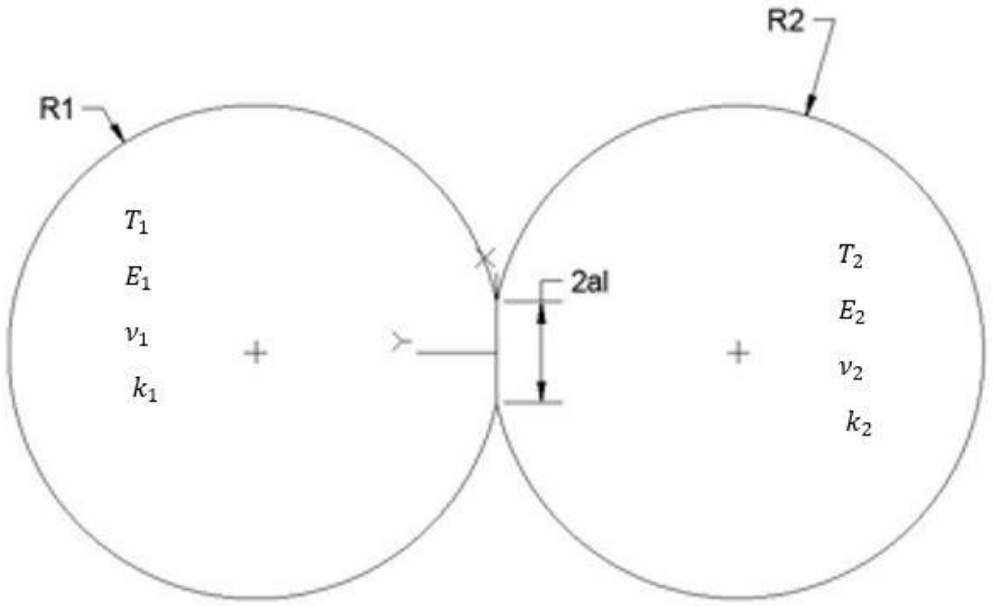

Figure 41: Schematic illustrates the case of two cylindrical filaments in contact laterally.

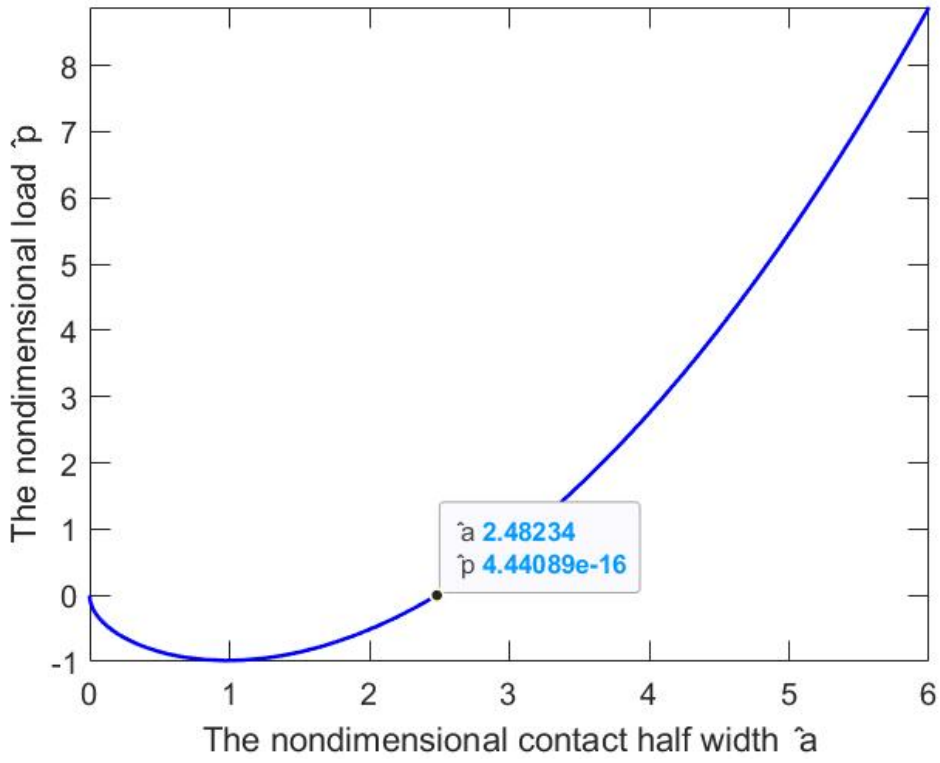

Figure 42: Plot of the normalized applied load as a function of the normalized contact half-width for PLA-PLA filament contact between 0.4 mm diameter filaments.

Appendix D: Summery for Contact Half-width Calculations

Table 4: Summary for the results of the contact half-width calculations for all the four contact cases and sub-parts

Case #:	Bodies in contact	Applied Force F (N)	Contact half-width. a (mm)	Diameter of 1^{st} body before contact D_1 (mm)	Diameter of 2^{ed} body before contact D_2 (mm)	Half-height of a single filament after contact. h (mm)	Change in filament height after contact. ΔH (mm)	Filament height after contact. H (mm)
Case 1	Ball – 1^{st}printed filament	0.2	0.037	12	0.2	0.093	0.014	0.186
Case 2 (contact under a load of ball weight)	Part 1: 1^{st} printed filament – 2^{nd} printed filament	0.2	0.075	0.2	0.4	0.185	0.029	0.37
	Part 2: 2^{nd} printed filament – 3^{rd} printed filament.	0.2	0.087	0.4	0.4	0.180	0.039	0.36
Case 1 + case 2	Four layers of filaments	-	--	-	-	-	0.121	1.279
Case 3 (contact under a load of upper filament weight with no swell effect)	Part 1: 1^{st} printed filament – 2^{nd} printed filament	0.00012	0.00831	0.2	0.4	0.0997	0.0007	0.1994
	Part 2: 2^{nd} printed filament – 3^{rd} printed filament.	0.00012	0.01012	0.4	0.4	0.1997	0.0006	0.3994
	Four layers of filaments	-	-	-	-	-	0.0025	1.3975
Case 3 (contact under a load of upper filament weight with swell effect)	Part 1: 1^{st} printed filament – 2^{nd} printed filament	0.00014	0.00874	0.2	0.44	0.0996	0.00077	0.1992
	Part 2: 2^{nd} printed filament – 3^{rd} printed filament.	0.00014	0.011	0.44	0.44	0.2197	0.0006	0.4394
	Four layers of filaments	-	-	-	-	-	0.0026	1.517
Case 4	Two printed filaments in contact laterally.	0	0.0056	0.4	0.4	0.1999	0.0002	0.3998

Appendix E: Illustration Figures for Meso-structure and Void Fraction

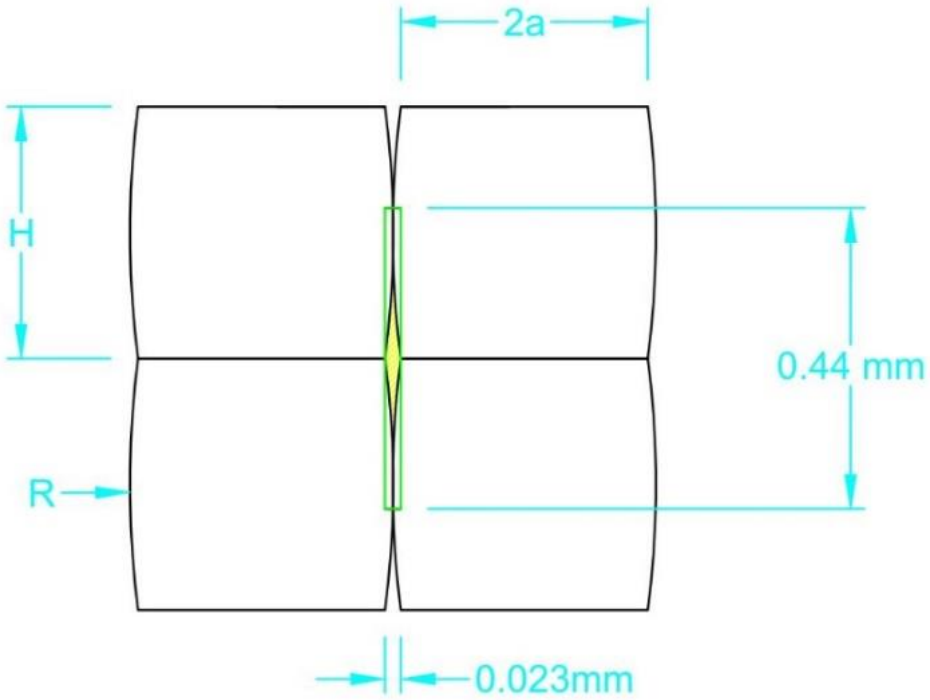

Figure 43: Illustration of the part predicted cross-section after applying rolling load.

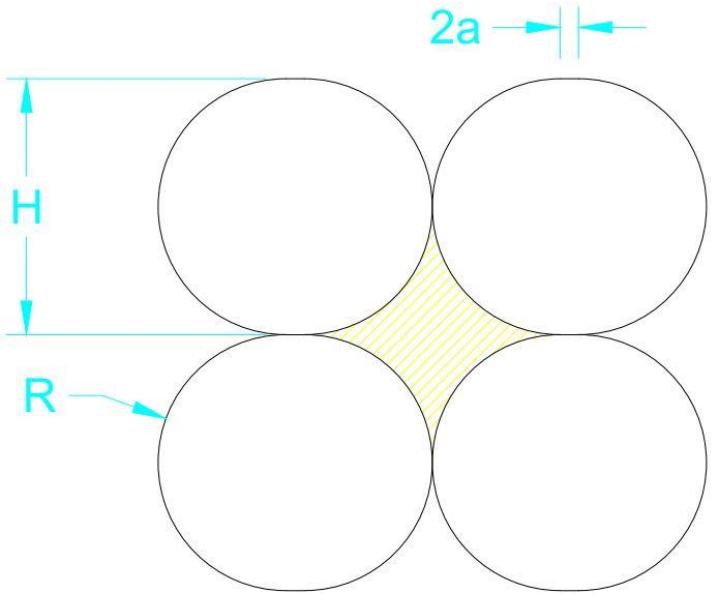

Figure 44: Illustration of the part predicted cross-section after applying filament weight load.

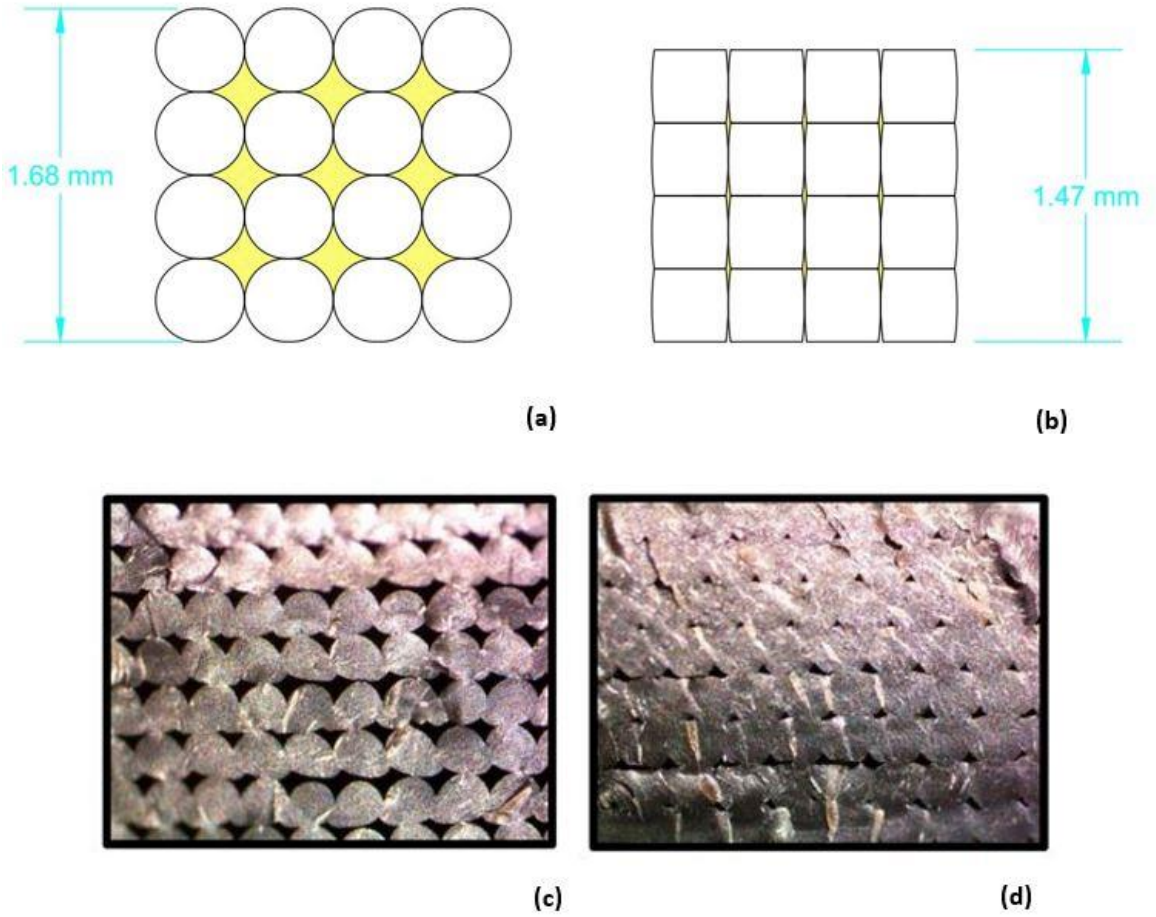

Figure 45: Schematics of (a) Predicted mesostructure for no rolling case. (b) Predicted mesostructure for ball rolling case. (c) Actual mesostructure for no rolling case. (d) Actual mesostructure for ball rolling case.

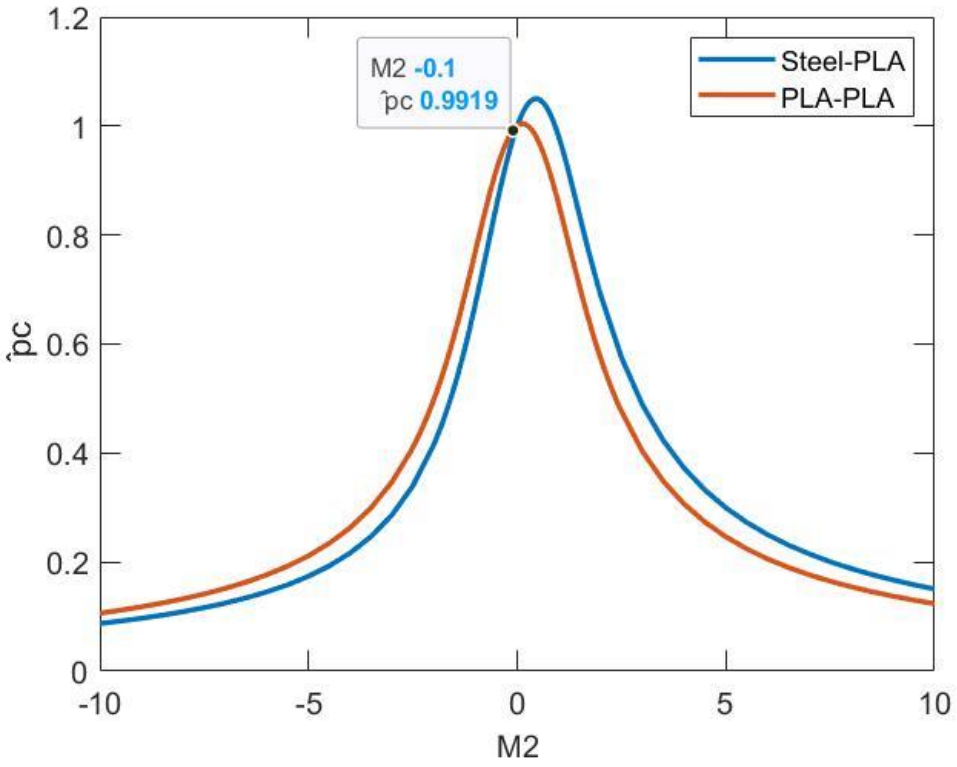

Figure 46: Plot of normalized pull-off force versus M_2 parameter.

$$\hat{P} = \frac{1}{3}\hat{a}^2 + \frac{4}{3}(2\pi^2)^{-1/3}\frac{M_2(B-1)}{C\,(B+1)}\hat{a} - \sqrt{\frac{16}{9}\hat{a} - \frac{4}{9}\left(\frac{\pi}{2}\right)^{\frac{2}{3}}(M_2\hat{a})^2} \tag{37}$$

Where,

$$M_2 = \left(\frac{E^*R^*}{\Delta\gamma}\right)^{1/3}(k^*(T_0^{(2)} - T_0^{(1)})(\delta_1 + \delta_2) \tag{38}$$

$$B = \frac{\delta_1}{\delta_2} \tag{39}$$

Then we define the pull-off force as: $\widehat{P_c} = \frac{P_c}{P_{IC}}$ which is corresponding to a_c the critical contact half-width. So,

$$\widehat{P_c} = \frac{P_c}{P_{IC}} = \frac{1}{3}\hat{a}_c{}^2 + \frac{4}{3}(2\pi^2)^{-1/3}\frac{M_2(B-1)}{C\,(B+1)}\hat{a}_c - \sqrt{\frac{16}{9}\hat{a}_c - \frac{4}{9}\left(\frac{\pi}{2}\right)^{\frac{2}{3}}(M_2\hat{a}_c)^2} \tag{40}$$

Therefore,

To find a_c we need to drive the previous equation and equate it to zero, then solve for a_c:

$$\frac{d\widehat{P_c}}{d\hat{a}_c} = \frac{2}{3}\hat{a}_c + \frac{4}{3}(2\pi^2)^{-1/3}\frac{(B-1)}{C\,(B+1)}M_2 - \frac{\frac{16}{9} - \frac{8}{9}\left(\frac{\pi}{2}\right)^{\frac{2}{3}}M_2{}^2\hat{a}_c}{2\times\sqrt{\frac{16}{9}\hat{a}_c - \frac{4}{9}\left(\frac{\pi}{2}\right)^{\frac{2}{3}}(M_2\hat{a}_c)^2}} = 0 \tag{41}$$